CO_2 condensation onto alkanes: Unconventional cases of heterogeneous nucleation

Journal:	*Physical Chemistry Chemical Physics*
Manuscript ID	CP-ART-02-2019-000967.R1
Article Type:	Paper
Date Submitted by the Author:	19-Mar-2019
Complete List of Authors:	Park, Yensil; The Ohio State Univeristy, William G. Lowrie Deptartment of Chemical and Biomolecular Engineering Wyslouzil, Barbara; The Ohio State University, William G. Lowrie Department of Chemical and Biomolecular Engineering; The Ohio State University, Department of Chemistry and Biochemistry

CO_2 condensation onto alkanes: Unconventional cases of heterogeneous nucleation

Yensil Park[1] and Barbara E. Wyslouzil[,1,2]

[1]William G. Lowrie Department of Chemical and Biomolecular Engineering, Ohio State University, Columbus, Ohio 43210, USA
[2]Department of Chemistry and Biochemistry, Ohio State University, Columbus, Ohio 43210, USA
Corresponding Author
*Email: wyslouzil.1@osu.edu (BEW)

ABSTRACT

The classical picture invoked for heterogeneous nucleation is frequently that of a liquid condensing onto an immiscible solid particle. Here, we examine heterogeneous nucleation of CO_2 onto particles comprised of n-pentane or n-hexane under conditions where CO_2 should be a solid and the seed particles may be liquid or solid. Although CO_2 condensed under all but one of the six conditions investigated, these experiments do not easily fit into the framework of standard heterogeneous nucleation experiments. Rather they explore unconventional regimes of heterogeneous nucleation in which the state of the seed particle may both affect whether deposition can proceed, and, in turn, be influenced by the presence of the condensing species. The work complements the earlier work of Tanimura et al. [RSC Advances, 2015, **5**, 105537-105550] that investigated CO_2 condensation onto ice nanoparticles, by using seed particles comprised of non-polar compounds that form and freeze under conditions where CO_2 is already supersaturated with respect to the solid ice. In some cases, the conditions for seed formation approach the limit of homogeneous CO_2 nucleation. Vibrational spectroscopy measurements help pinpoint where CO_2 starts to condense. Furthermore, these IR measurements suggest that the n-alkanes never freeze in the presence of CO_2, even if the temperatures are well below those required for them to freeze when CO_2 is absent. Over the temperature range $65 < T/K < 140$, the conditions corresponding to the onset of CO_2 heterogeneous nucleation on pre-existing seed particle almost all lie very close to the extrapolated vapor-liquid equilibrium line of CO_2 for a broad range of seed materials.

I.   INTRODUCTION

The critical role particles play in initiating condensation in most real life situations has been recognized since Wilson[1] made the first measurements to determine the extent to which moist air could be expanded in the absence of particles. To date, heterogeneous nucleation research has been largely motivated by the need to understand the conditions for existing aerosol particles (cloud condensation nuclei) to nucleate and grow to form cloud droplets at the relatively low water supersaturations (1.01 – 1.02) present in tropospheric clouds.[2] At lower temperatures, ice is the stable phase of water and the equivalent question is what determines whether aerosol particles act as good ice condensation nuclei.[3] Experiments show that only very specific aerosol particles (certain mineral dusts), can initiate ice deposition close to the solid-vapor equilibrium line.[3] Most other particles require a higher degree of supersaturation, and in some cases, water vapor may not deposit as ice until the partial pressure of water reaches the liquid-vapor saturation line.[3, 4] In the latter case, liquid water condenses before the particle freezes and growth continues via deposition.

Other heterogeneous nucleation studies[5-12] are motivated by the need to develop instrumentation to detect molecular ions and particles as small as 1 – 2 nm. These instruments – Condensation Particle Counters (CPCs) – use working fluids such as water or butanol, to grow nanometer size particles into the micron size range needed to detect them via light scattering. Typical supersaturations in these devices are on the order of 1.5 – 3, and the condensate is always in the liquid state. Detecting the smallest particles, independent of their composition, means increasing the supersaturation and runs the risk of creating new particles via homogenous nucleation. Thus, continued development of these devices requires a robust understanding of heterogeneous vs homogeneous nucleation.

Heterogeneous nucleation in supersonic or high speed flows is a largely unexplored area of research.[13-15] In part, this is because heterogeneous nucleation in supersonic nozzle flows only competes successfully with homogeneous nucleation if the seed particle number densities are greater than about $10^6 - 10^7$ cm^{-3}.[15, 16] Nevertheless, understanding heterogeneous nucleation under these highly non-equilibrium conditions is important for a wide range of technological applications. In particular, supersonic separators have been proposed as a route to process intensification.[17] Here, the basic idea is to combine (1) a supersonic expansion to cool the gas and induce droplet formation and growth with (2) inertial separation to capture the condensate, and (3) a diffuser to recompress the residual gas and minimize the overall pressure loss. Applications include removing water and higher hydrocarbons from natural gas,[18, 19] purifying and separating H_2 from coal derived syngas,[17] and recovering CO_2 from flue gas.[20, 21] In most of these separation schemes, there are multiple condensable species that are either highly immiscible[22] or have vapor pressures that differ by orders of magnitude.[17] Thus, true binary homogeneous nucleation is unlikely to play a role in initiating the phase transition. Rather, one species condenses first, followed by heterogeneous nucleation and condensation of other condensable vapor(s) onto these seeds. Understanding the competition between homogeneous and heterogeneous nucleation/condensation is, therefore, also critical to separator design.

In the particular case of CO_2 removal from "dehydrated" flue gas, water vapor is likely still present at levels high enough to form particles while the saturation S_{CO2} of CO_2(g) with respect to the solid is less than 1. Thus, once S_{CO2} is high enough to initiate a phase transition, CO_2 condensation should proceed by heterogeneous nucleation and growth onto ice, rather than by homogeneous nucleation of CO_2 itself. Tanimura et al.[23] investigated these ideas by studying

heterogeneous nucleation of CO_2 onto small ice particles in a supersonic nozzle. The ice particles, with radii of gyration from 2.1 to 4.3 nm and number densities on the order of ~10^{13} cm^{-3}, were made by vapor to liquid ($v \rightarrow l$) homogeneous nucleation of water near the throat of the nozzle. The water droplets grew by condensation and froze well before CO_2 started to condense, and CO_2 only condensed in the nozzle when water particles were present. For temperatures between 131.0 and 143.8 K, the critical supersaturations, S_{CO2}^* required to initiate heterogeneous nucleation were between 6.4 and 8.2. Furthermore, the onset of heterogeneous nucleation of CO_2 was a function of the size of the initial particle and consistently occurred near the extrapolated vapor-liquid phase equilibrium line. This observation suggested that CO_2 vapor may have first condensed as a supercooled liquid before freezing to form solid CO_2.

In this paper, we extend Tanimura et al.'s study of CO_2 heterogeneous nucleation[23] in two important ways. First, we change the nature and size of the seed particles. Specifically, n-pentane and n-hexane are used to produce seed particles because (1) the molecular interactions between the n-alkane seed particles and CO_2 should be quite different from those between water and CO_2, (2) n-alkane seed particles can be larger than water seed articles in part because the n-alkane molecules are much larger than water molecules, (3) n-pentane and n-hexane condense and freeze at much lower temperatures than water, and, thus, we can potentially explore the transition between heterogeneous and homogeneous nucleation as well as the effect of using solid versus liquid seed particles. The second change was to measure position resolved IR spectra in order to follow the phase transitions in more detail, to try to identify the state – vapor, liquid, or solid – of each condensable species, and thereby gain additional insight into the mechanism of heterogeneous nucleation of CO_2 on the micro-second time scale.

Although CO_2 condensed under almost all of the conditions investigated, these experiments do not easily fit into the framework of standard "heterogeneous" nucleation experiments – that of a liquid seed forming on a preexisting solid particle.[24] Nor are they as straightforward as the CO_2 – ice experiments of Tanimura et al.[23] where the seed particles were solid before CO_2 deposited. Rather they explore "unconventional" regimes of heterogeneous nucleation in which the state of the seed particle may both affect whether deposition can proceed and, in turn, be influenced by the presence of the condensing species.

II. EXPERIMENTAL

A. The Flow System

Experiments were conducted using the flow system detailed in Tanimura et al.[23] In the current experiments the carrier gas, Ar, is drawn from the gas side of two liquid Dewars, and CO_2 is either drawn from the gas side of a Dewar or supplied from a high pressure bottle (bone dry). The gases are heated to room temperature, and their flow is controlled by mass flow controllers. A peristaltic pump forces the liquid n-alkane into the vaporizer where it is evaporated by spraying into a heated Ar stream. The flowrate of liquid entering the system is monitored using a balance. The mixture of Ar, CO_2 and vaporized n-alkane flows through a plenum where the stagnation temperature (T_0) and stagnation pressure (p_0) reach their desired values before entering the supersonic nozzle. Once in the nozzle, the flow accelerates, expands, and cools at a rate of ~1.1K/μs for the first ~60 μs. Flow through the nozzle is maintained by two rotary vane pumps with a combined pumping capacity of 0.2 m^3/s.

The nozzles used in these experiments, denoted T1W and T1W_mica, have the same shape as Nozzle T1 used by Taninimura et al.[23] but are 12.7 mm rather than 6.4 mm wide. The main difference between the two versions of the nozzle used here was the window material used in the sidewall. Nozzle T1W had 3 mm-thick CaF_2 windows, whereas nozzle T1W_mica had 25 μm-thick mica windows. The effective area ratios of the nozzles are essentially identical (Figure S1, Supplemental Information).

B. Pressure Trace Measurements (PTM)

In the expanding nozzle flow, aerosols can form via homogeneous nucleation and evolve via condensational growth, coagulation, and, potentially heterogeneous nucleation. Liquid droplets can also freeze to form solids. Both condensation and freezing can release enough heat to the flow to increase its temperature and static pressure above that expected for an isentropic expansion. Static pressure measurements can, therefore, detect and begin to quantify these phase transitions. In a PTM, we measure both the inlet conditions, and the static pressure along the centerline of the nozzle with ~2 mm resolution using a thin, movable pressure probe. As detailed in the Analysis section, II.E, the pressure data – alone, or in combination with the results of other techniques – are used to estimate the other properties of the expansion, in particular the effective area ratio of the expansion (A/A^*), the temperature (T), density (ρ), and velocity (u) of the flow, and the mass fraction of condensate (g).

C. Small Angle X-Ray Scattering (SAXS)

Although PTMs can detect phase transitions, they cannot characterize the particle size distribution or number density of the resulting aerosol. Nor can they follow processes like coagulation that do not release heat to the flow. Since we are interested in the effect of seed particle size on heterogeneous nucleation, we used SAXS to follow aerosol evolution in more detail.

SAXS experiments were conducted using the 12-ID_C beam line at the Advanced Photon Source (APS), Argonne National Laboratories, Argonne, IL.[25] For these measurements, we used the T1W_mica nozzle to minimize parasitic scattering from the windows as the X-rays pass

through the nozzle. The nozzle and plenum were mounted on a translation stage to enable position resolved measurements. An X-ray wavelength of $\lambda = 0.1$ nm and sample-to-detector distance of 2.25 m yielded an appropriate q-range for the given particle sizes, where $q = (4\pi/\lambda)$ $\sin (\theta/2)$ and θ is the scattering angle. At each position 10 X-ray shots, each $0.3 - 0.8$ s long, were taken for the sample and then again for the background. The two-dimensional scattering data were converted to one-dimensional spectra using the APS data inversion program, and then averaged. After background subtraction, the averaged one-dimensional data can be fit to scattering models corresponding to particles with different shapes, structures, and degrees of polydispersity. Here, the data are fit assuming the aerosol comprises spherical particles that follow a Schulz size distribution.[26, 27] The fit parameters returned are the mean particle size $\langle r \rangle$, the distribution width σ, and the intensity at $q = 0$, I_0. As illustrated in Figure S2, the fits to the measured SAXS spectra are generally very good.

D. FTIR

When temperatures in the nozzle are cold enough that droplets can freeze or CO_2 can condense, the state and average composition of the aerosol is required to analyze the PTM and SAXS data correctly. We therefore conducted FTIR measurements using the setup, illustrated in Figure 1, that is designed to minimize the interference from CO_2 in the room air. It consists of 1 plane mirror and 2 focusing mirrors that guide the IR beam from the Perkin Elmer Spectrum 100 to the external MCT detector. To analyze the alkane spectra, we apply the Beer-Lambert law, and assume that the total absorbance is a linear combination of the absorbance of each phase. A least squares fit to the total absorbance determines the concentrations of each phase, or equivalently, the mass fractions of alkane in each phase: vapor (g_v), liquid (g_l), and solid (g_s) phase. This approach requires the normalized absorptivities of the vapor (ε_v), liquid (ε_l), and solid (ε_s) phases of the alkane, and these were determined as described in detail in Modak et al.[28, 29] To summarize briefly, the normalized absorptivity of vapor phase is determined from spectra measured upstream of the onset of condensation. If the droplets do not freeze, the normalized absorptivity of the liquid is based on absorption measurements near the nozzle exit and the mass fraction of condensate based on the integrated PTM/SAXS analysis. If the aerosol freezes, the normalized absorptivity of the solid is based on measurements near the nozzle exit, and that of the liquid comes from measurements prior to freezing in the same experiment, or from a separate experiment where freezing did not occur.

For CO_2, prior to condensation the measured FTIR spectra can be understood and validated by modeling the experiment using the online spectral calculator available at SpectralCalc.com. This program uses the HITRAN 2016 data base to predict the absorbance spectra of gas phase molecules under user defined conditions. As illustrated in Figure 1, the FTIR experiment can be thought of as two gas cells in series. The first cell corresponds to the path of the beam through the atmosphere. Light transmitted through this cell corresponds to the intensity of the background. For our experiments, we assumed this cell contains air at atmospheric pressure (101.325 kPa) and temperature (296 K) with a CO_2 volume mixing ratio of 400 ppm (the typical amount of CO_2 in atmospheric air) and has a path length of ~88 cm. The second cell is the nozzle. Light transmitted though both cells corresponds to the intensity of the sample. The pressure and temperature conditions in the second cell are those estimated from the PTM, a CO_2

mixing ratio of 0.12 – 0.14, and a pathlength of 1.27 cm. Since the FTIR is not a high-resolution instrument, we apply a Gaussian line shape with a width of 1.2 cm^{-1}.

The FTIR determines the absorbance by measuring the intensity of the light transmitted along the path in the presence of the sample (intensity of sample) and in its absence (intensity of background). The absorbance is then,

$$\text{Absorbance} = -\log_{10} \text{Transmittance} = -\log_{10} \frac{\text{Intensity of sample}}{\text{Intensity of background}} \qquad (1)$$

To simulate the FTIR signal, we calculated the spectra corresponding to the sample and the background, then determined the absorbance using Eq. (1). Once CO_2 starts to condense, the experimental CO_2 signal between 2250 cm^{-1} and 2400 cm^{-1} deviates distinctly from that predicted by the model for gas phase CO_2.
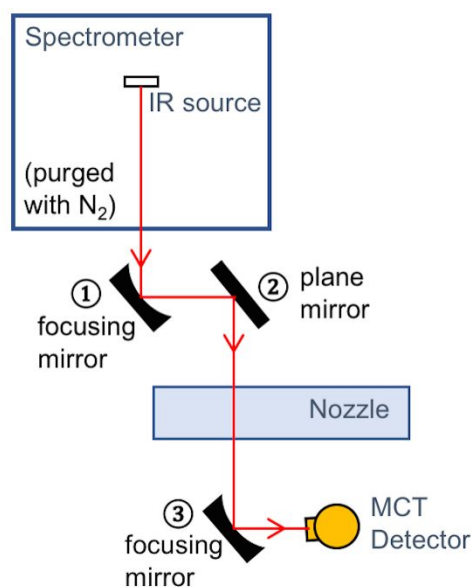
Figure 1. A schematic top view of the FTIR experimental setup. The IR beam exits the spectrometer (Perkin Elmer 100) via the side window, and is guided through the nozzle and onto the external Mercury Cadmium Telluride (MCT) detector using two focusing mirrors (focal length: ①=15cm and ③=5.6cm), and one plane mirror (②). The inside of the spectrometer, ~38 cm of the path length, is purged with N_2 gas and ~50 cm of the path length passes through the room air. The effective sample path length is the width of the nozzle, 1.27 cm. The spectra were collected using the spectrum 10 software from Perkin Elmer without using the option to remove atmospheric CO_2 and water absorption lines.

E. Integrated Data Analysis

Depending on the number of species and the complexity of the phase transitions involved, different approaches are used to analyze the combined data in the most self-consistent manner possible, as outlined below.

Method 1: Vapor-liquid phase transition of an alkane

When only a single vapor condenses to the liquid state, we use the integrated analysis approach developed in our earlier work.[30] In particular, the 4 equations that describe flow in the nozzle in the presence of condensation, i.e. mass balance, momentum balance, energy balance, and an equation of state, involve 6 variables – pressure (p), temperature (T), density (ρ), velocity (u), area ratio (A/A^*), and mass fraction of condensate (g). To determine all the variables, we need to know or measure two of them and solve the 4 equations to estimate the others.

In PTM experiments, we measure p in the absence (carrier gas only) and presence (carrier gas + condensable material) of the condensable species. If we assume that the area ratio (A/A^*) of the dry (carrier gas only) and wet (carrier gas + condensable material) trace are the same, we can determine first estimates for T, ρ, u and g. We then conduct SAXS measurements and, based on the initial estimates for T and ρ, get a second estimate for g from the mean particle size $\langle r \rangle$, particle size distribution width σ, and scattering intensity I_0. The mass fraction of the condensate of a given phase can be calculated as

$$g_i = \frac{\rho_i}{\rho}\phi \tag{2}$$

where subscript i denotes the phases, i.e. liquid (l) or solid (s), ρ_i is the mass density of the condensate, ρ is the mass density of the gas mixture, and ϕ is the volume fraction of condensate. Here, $g_i = g_l = g$ and $\rho_i = \rho_l$ since this method only considers the vapor to liquid phase transition.

For polydisperse spherical particles that follow a Schulz distribution,[26] ϕ can be obtained from the fit parameters using[27]

$$\phi = \frac{3}{4\pi\Delta\rho_{SLD}^2} \frac{I_0}{\langle r \rangle^3} \frac{(Z+1)^3}{(Z+6)(Z+5)(Z+4)} \tag{3}$$

where

$$Z = \left(\frac{\langle r \rangle}{\sigma}\right)^2 - 1 \tag{4}$$

and $\Delta\rho_{SLD}$ is the scattering length density difference between the condensate and the gas mixture. This estimate for g is then used with p to recalculate all the variables using the 4 flow equations. The new values of T and ρ are then used to reanalyze the SAXS data and iteration continues until

the calculated variables converge, usually in 2-3 trials. The initial PTM analysis underestimates g and T because it cannot account for changes to the boundary layer due to heat addition.[30] We denote the initial temperature estimate – based on PTM alone – as T_{PTM} and that based on iteration as T_{int}. Under the operating conditions used here, we estimate that at the nozzle exit the main flow occupies ~75-80% of the available flow area.

Method 2: Vapor-liquid and liquid-solid phase transitions of n-alkane

When flow temperatures are low enough that liquid droplets can freeze, as in the n-hexane experiments, we follow the approach of Modak et al.[28, 29] We first analyze the PTMs alone assuming that freezing has not occurred. As in Method 1, we then analyze the SAXS data to get the initial estimates of g_l and g_s assuming the particles at the last 2-3 points are fully frozen, and those at other points are still purely liquid. We then determine the normalized absorptivities for each phase, ε_v, ε_l, and ε_s, based on the FTIR absorbance measurements and the g_l and g_s estimates from PTM/SAXS, at carefully selected positions. In particular, ε_v is determined from spectra measured upstream of condensation, ε_l is determined from spectra measured near the onset of condensation prior to freezing, and ε_s from the last 2 -3 points where the aerosol appears fully frozen. Least squares fitting of all of the absorbance measurements determines the concentration of each phase, or equivalently, the mass fraction of each phase as a function of position. The g_l and g_s values, together with p, are then used to solve the standard flow equations modified to include the heat release associated with the second phase transition. We then repeat all of the calculations until the solution converges, usually in 2-3 iterations.

Method 3: Heterogeneous nucleation of CO_2 onto n-alkane particles

When two species condense, either simultaneously or sequentially, the composition of the evolving aerosol is required in order to correctly estimate the heat release. One way to do this is to include a model that relates the composition of the aerosol to that of the gas phase. If heterogeneous nucleation of CO_2 is initiated well after condensation of the first species (alkane), it is possible to assume the first heat release is strictly due to the alkane and the second heat release is due only to CO_2. If species condense simultaneously, a simplistic approach is to set the composition of the condensed phase equal to that of the gas mixture. Finally, a more sophisticated approach is to assume thermodynamic equilibrium between the vapor and condensed phases. In particular, we assume that

$$\frac{y_1}{y_2} = \frac{p_1^{mix}(T, x_1^{av})}{p_2^{mix}(T, x_1^{av})} = \frac{x_1^{av} \gamma_1 p_{e,1}(T)}{x_2^{av} \gamma_2 p_{e,2}(T)} \tag{5}$$

where, for species j = 1 (alkane) or 2 (CO_2), y_j is the vapor phase mole fraction, $p_j^{mix}(T, x_j^{av})$ is the partial pressure of that species above a mixture at temperature T with average composition x_j^{av}, γ_j is the activity coefficient, and $p_{e,j}(T)$ is the equilibrium vapor pressure. Given the lack of thermodynamic data, we set $\gamma_1 = \gamma_2 = 1$.

IR spectroscopy has also been used to directly determine the distribution of two species between the vapor and condensed phases.[31] These studies clearly showed that the simplistic model of co-condensation based on the initial vapor composition is not realistic. Although we would prefer to use IR spectroscopy to directly measure of the distribution of species between the vapor and condensed states, the calibration methods required to determine the extent of CO_2 condensation are not yet in place. Since the wavenumber range for the C–H vibrational bands is far from that of the antisymmetric vibrational C–O band, we can detect condensed n-alkane present in the binary particles and, potentially, determine whether it is crystalline or not.

In summary, we used method 1 to analyze n-pentane unary condensation and method 2 to analyze n-hexane unary condensation. For binary systems, we followed Tanimura et al.[23] and used the PTM alone together with Eq. (5) unless it was clear that CO_2 did not condense. Where appropriate, we then adjusted T_{PTM} in the binary flows by adding the correction $\Delta T = T_{int} - T_{PTM}$ observed for the corresponding unary experiment. Although this is an *ad hoc* correction, it accounts for the expected change in the boundary layer due to comparable heat release for the n-alkane and should be more accurate than simply ignoring this effect.

F. Materials

Liquid argon, with purity of 99.998%, was purchased from Praxair. The n-pentane was purchased from Sigma Aldrich and the n-hexane from ChemSampCo. Both had purity > 99 % and were used as received. The thermophysical properties used in the data analysis are in Table A-1.

III.   Results and Discussion

To appreciate the complexity of the experiments we start by examining the phase diagrams of CO_2, hexane and pentane (Figure 2). For clarity, only the *v-l* equilibrium lines and the triple points are plotted for the *n*-alkanes. This is reasonable because the recent work of Ogunronbi et al.[32] suggests that at the onset of condensation the critical clusters controlling the alkane $v \rightarrow l$ nucleation are still liquid-like despite the high degree of supercooling. The conditions corresponding to homogeneous $v \rightarrow l$ nucleation of *n*-hexane, *n*-pentane and CO_2, as well those corresponding to heterogeneous nucleation of CO_2 on ice are indicated by the symbols. For CO_2, we extrapolated the high temperature condensation data measured by Duff[33] into our temperature range, by fitting his data to $\log p = c_1/T + c_2$. This fit is motivated by the observations that in constantly expanding supersonic nozzles, the conditions corresponding to the maximum
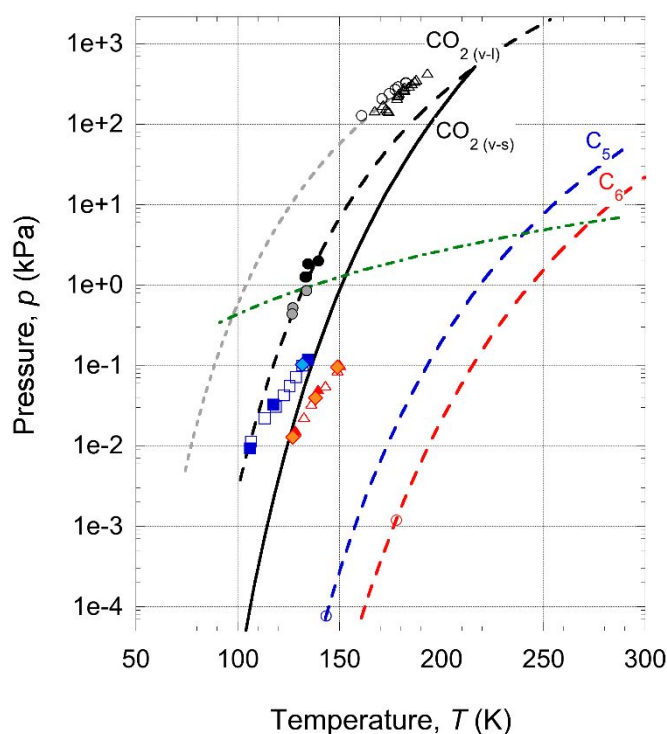
Figure 2. The equilibrium phase boundaries for the solid-vapor (solid black line) or liquid-vapor regions (long dashed lines) and triple points (red/blue open circles) are indicated on a combined phase diagram for CO_2 and the *n*-alkanes. Conditions corresponding to the homogeneous nucleation of the *n*-alkanes and CO_2 in supersonic flows are indicated by the symbols: CO_2 (open black circles and triangles[33]), *n*-pentane (open[32] and filled blue squares), *n*-hexane (open[32] and filled red triangles). The filled squares, triangles and diamonds are from the current work, where the diamonds indicate the onset of alkane condensation in the presence of CO_2. The short dashed line is the extrapolation of Duff's CO_2 results into our temperature regime. Filled black/grey circles are the onset of heterogeneous nucleation of CO_2 onto water ice nanoparticles for $y_{CO2,0}$ = 0.14 and 0.07, respectively.[23] The green dash-dot line traces the *p-T* history of CO_2 as a mixture with $y_{CO2,0}$ = 0.12 expands across the nozzle in the absence of condensation.

nucleation rate data lie along a straight line when $\log p_{Jmax}$ is plotted as a function of $1/T_{Jmax}$ (see Figure A1), and the maximum nucleation rate is reached shortly after the point where particles first appear.[32, 34] Assuming the onset pressures and temperatures reported by Duff are close to the conditions corresponding to the maximum nucleation rate, this fit is a good way to extrapolate his data into our temperature range.

Several key points can be gleaned from this diagram. First, the vapor pressure of the alkanes is ~4 orders of magnitude lower than that of CO_2. Nevertheless, the high degree of supersaturation required to induce $v \rightarrow l$ nucleation of the n-alkanes means that under these operating conditions (1) the n-alkanes begin to condense in the same temperature range that CO_2 nucleated heterogeneously onto small ice particles, and (2) CO_2 is already supersaturated with respect to the solid when n-hexane starts to condense and with respect to the supercooled liquid when n-pentane starts to condense. Thus, if the interactions between the molecules is favorable enough, some of these experiments could lead to particle formation via binary nucleation rather than via heterogeneous nucleation. Furthermore, the presence of CO_2 could either enhance freezing of the n-alkanes by acting as a heterogeneous seed particle,[35-37] or hinder freezing by dissolving in the n-alkane thereby lowering the melting point.

To explore the wide range of possibilities, experiments were conducted for gas mixtures at 3 different mole fractions of n-pentane and n-hexane in the presence and absence of ~12 mol% CO_2. The value of CO_2 was chosen to be close to one of the cases used by Tanimura et al.[23] and is in the range of typical CO_2 concentrations in flue gas,[38] between 7 and 30 mol%. The n-alkane conditions were chosen to span as wide a range of conditions as feasible. Table 1 summarizes the experimental conditions.

Table 1. The experimental conditions investigated are defined by the mole fractions of n-alkane ($y_{C5,0}$, $y_{C6,0}$) and CO_2 ($y_{CO2,0}$). All experiments started at a stagnation pressure $p_0 = 60.5$ kPa and stagnation temperature $T_0 = 293.15$K.

n-hexane			n-pentane		
$y_{C6,0}$	$y_{CO2,0}$	Symbol	$y_{C5,0}$	$y_{CO2,0}$	Symbol
0.0026	0	LF_{C6}	0.0024	0	LF_{C5}
0.0026	0.110	$LF_{C6}+CO_2$	0.0025	0.120	$LF_{C5}+CO_2$
0.0055	0	MF_{C6}	0.0055	0	MF_{C5}
0.0055	0.110	$MF_{C6}+CO_2$	0.0058	0.119	$MF_{C5}+CO_2$
0.0101	0	HF_{C6}	0.0158	0	HF_{C5}
0.0104	0.109	$HF_{C6}+CO_2$	0.0162	0.109	$HF_{C5}+CO_2$

A. Identifying the sequence of phase transitions

PTM experiments were performed at each experimental condition to determine both the sequence and the conditions corresponding to the relevant phase transitions. For the n-alkane experiments, the PTM data were combined with SAXS/FTIR measurements using the integrated

data analysis approach, i.e. method 1 or 2 of Section II.E. For the alkane – CO_2 measurements, the data were analyzed using pressure measurements alone, i.e. using method 3, as described in Section II.E and, where feasible, temperatures were corrected based on the pure alkane condensation experiments.

Figures 3 and 4 summarize the pressure and calculated temperature profiles for n-hexane and n-pentane in the absence and presence of CO_2. In all experiments, the pressure trace for the condensing flow follows that of the expected isentropic expansion of the gas mixture until a sudden increase in the pressure and temperature, that stems from the heat release associated with particle formation and growth, indicates the first phase transition, i.e. the condensation of alkane from the vapor phase. For n-hexane alone, there is a second "bump" in the PTM – near z = 4.9 cm in Figure 3(c), and near z = 6.0 cm in Figure 3(e), that corresponds to the initiation of droplet freezing as confirmed in FTIR measurements (Section III.C). It is difficult to detect this second bump in Figure 3(a) because for the LF_{C6} condition the amount of heat released by freezing is too small for the given carrier gas pressure and expansion rate. Droplet freezing is, however, observed at LF_{C6} in the FTIR measurements (Section III.C). For n-pentane, Figures 4(a), (c), and (e) show that once the alkane condenses, the pressure and temperature again follow an isentropic expansion and there is no evidence for a second phase transition. For the pure alkane condensation experiments, both the initial (T_{PTM}, based on PTM only) and the iterated (T_{int}, based on integrated PTM+FTIR analysis) temperature estimates are shown. The largest differences between T_{int} and T_{PTM} are still less than 6 K and correspond to the highest alkane flowrates (HF_{C6} or HF_{C5}). Iteration was not attempted when CO_2 condensed, because we could not accurately quantify the amount of condensed CO_2. Instead, the temperatures were corrected manually as described in Section II.E, assuming boundary layer development was close to that when the pure alkane condensed.

Upon the addition of CO_2 to these flows, several changes are readily apparent. First, adding CO_2 reduces the mixture's heat capacity ratio and, therefore, the slower cooling rate leads to an isentropic temperature that is ~8.5 K higher at the nozzle exit. Consequently, the onset of the $v \rightarrow l$ phase transition shifts slightly downstream when CO_2 is present. Nevertheless, as summarized in Table 2, the temperatures T_{Jmax}, pressures p_{Jmax}, and supersaturations S_{Jmax}, corresponding the maximum vapor-liquid nucleation rates J_{max} of the alkanes appear unchanged by the presence of the CO_2. Furthermore, as illustrated in Figures 2 and A-1, the $v \rightarrow l$ phase transition measurements agree well with those reported by Ogunronbi et al.,[32] despite differences in carrier gas composition and a factor of 2 difference in carrier gas pressures. Thus, it is safe to conclude that the presence of CO_2 does not strongly affect the initial $v \rightarrow l$ phase transition, i.e. alkane nucleation controls the onset of condensation and binary nucleation is not an important source of particles in these experiments.
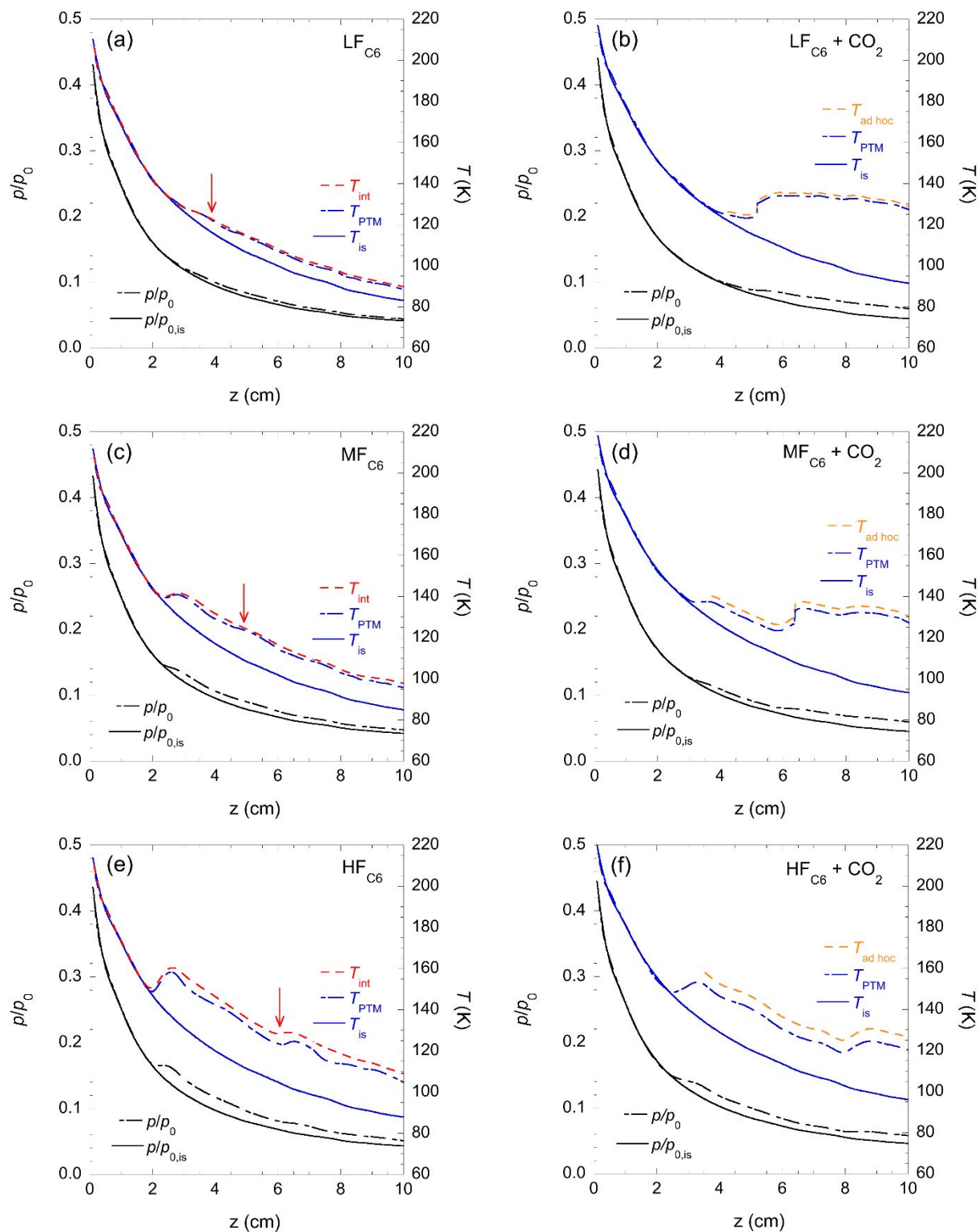
Figure 3. Pressure and temperature profiles for (a) LF_{C6} (b) $LF_{C6}+CO_2$ (c) MF_{C6} (d) $MF_{C6}+CO_2$ (e) HF_{C6} and (f) $HF_{C6}+CO_2$. Here, T_{is} is the temperature expected for an isentropic expansion of the gas mixture in the absence of any phase transitions and T_{PTM} is the temperature estimate

based on PTM alone. In the absence of CO_2, T_{int} is the temperature estimate from the integrated analysis approach and the arrow indicates the position where a rapid phase transition from liquid to solid starts. In the presence of CO_2, $T_{ad\ hoc}$ is based on T_{PTM} corrected for the temperature difference (T_{int}-T_{PTM}) observed in the equivalent experiments without CO_2 ($LF_{C6}+CO_2$: 1.5 K, $MF_{C6}+CO_2$: 3 K, $HF_{C6}+CO_2$: 6 K).
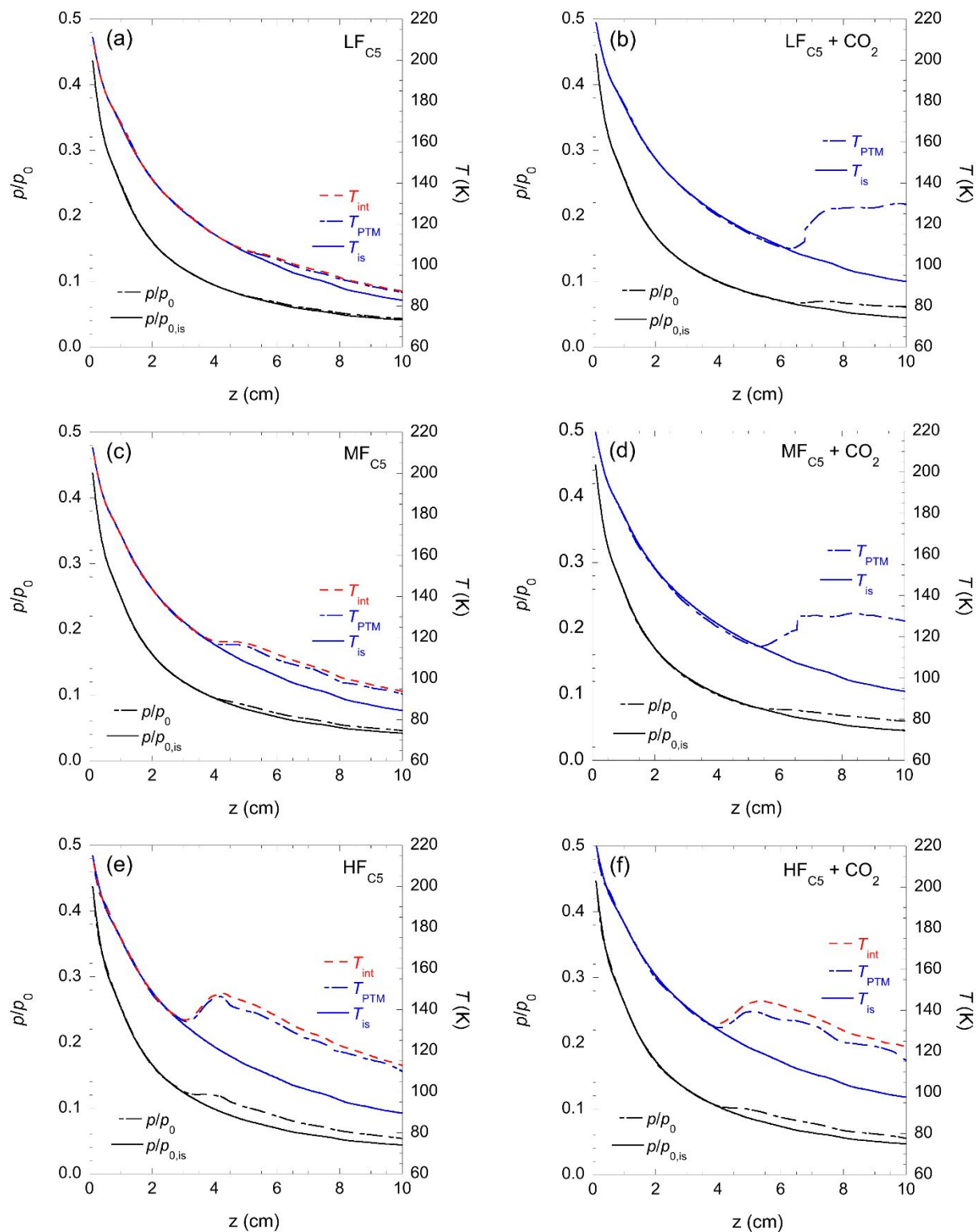
Figure 4. Pressure and temperature profiles for (a) LF$_{C5}$ (b) LF$_{C5}$+CO$_2$ (c) MF$_{C5}$ (d) MF$_{C5}$+CO$_2$ (e) HF$_{C5}$ and (f) HF$_{C5}$+CO$_2$. T_{is} is the temperature expected for an isentropic expansion of the gas mixture in the absence of any phase transitions, T_{PTM} is the temperature estimate based on

PTM alone, and T_{int} is the temperature estimate from the integrated analysis approach. T_{int} in (f) is calculated assuming CO_2 does not condense.

Table 2. The temperatures T_{Jmax}, pressures p_{Jmax}, and supersaturations $S_{\text{Jmax}} = p_{\text{Jmax}}/p_v^e(T)$ corresponding to the maximum $v \rightarrow l$ nucleation rates of the n-alkanes; $p_v^e(T)$ is the equilibrium vapor pressure with respect to the supercooled liquid. The rates were calculated using number densities measured shortly after the onset of condensation ($J_{\text{max|onset}}$) or at a fixed position ~7 cm downstream of the throat ($J_{\text{max|7 cm}}$). Nucleation rates were calculated as described in Ogunronbi et al.[32]

Experiment	T_{Jmax} (K)	p_{Jmax} (Pa)	S_{Jmax}	$J_{\text{max}}|_{\text{onset}}$	$J_{\text{max}}|_{7\text{cm}}$
LF$_{\text{C6}}$	128.4	15.5	4.80×10^5	2.17×10^{17}	2.17×10^{17}
LF$_{\text{C6}}$+CO$_2$	127.0	12.8	7.12×10^5	3.85×10^{17}	-
MF$_{\text{C6}}$	140.1	50.2	5.62×10^4	1.76×10^{17}	1.72×10^{17}
MF$_{\text{C6}}$+CO$_2$	138.1	39.5	8.25×10^4	1.89×10^{17}	-
HF$_{\text{C6}}$	149.0	105.6	1.59×10^4	1.55×10^{17}	1.15×10^{17}
HF$_{\text{C6}}$+CO$_2$	149.0	94.8	1.44×10^4	8.22×10^{16}	5.11×10^{16}
LF$_{\text{C5}}$	106.0	9.32	4.50×10^6	1.07×10^{17}	8.41×10^{16}
MF$_{\text{C5}}$	117.6	32.6	2.81×10^5	1.09×10^{17}	5.77×10^{16}
HF$_{\text{C5}}$	134.5	116.9	1.07×10^4	4.19×10^{16}	2.34×10^{16}
HF$_{\text{C5}}$+CO$_2$	131.8	102.7	1.78×10^4	3.24×10^{16}	1.62×10^{16}

The presence of CO_2 does, however, significantly change the shape of the subsequent temperature profiles for both n-alkanes. In the case of LF$_{\text{C6}}$+CO$_2$ and MF$_{\text{C6}}$+CO$_2$ there are two distinct temperature increases as shown in Figure 3(b) and (d). The first temperature increase corresponds to n-hexane particle formation and the second one to CO_2 condensation onto the n-hexane particles. Thus, these experiments correspond to heterogeneous nucleation onto preexisting, fully grown hexane particles. It is not clear from the pressure trace measurements, however, how large the particles are when CO_2 starts to condense or whether heterogeneous nucleation occurred on solid or liquid alkane particles. In particular, the temperature at which CO_2 appears to condense on the n-hexane particles is quite close to that where the pure particles froze. At the highest n-hexane flowrate, Figure 3(f), it is not clear whether the second heat addition is due to freezing alone, CO_2 condensation alone, or a combination of the two.

In contrast, in the cases of LF$_{\text{C5}}$+CO$_2$ and MF$_{\text{C5}}$+CO$_2$, Figures 4(b) and 4(d), the temperature increase is monotonic but distinctly larger than when n-pentane is the only condensable, Figure 4(a) and 4(c). The increased heat release suggests that n-pentane and CO_2 condense essentially simultaneously, i.e. as soon as n-pentane particles appear, CO_2 can condense onto them. This behavior is consistent with the phase diagram that shows CO_2 is supersaturated with respect to

the solid and, potentially, the supercooled liquid under the conditions corresponding to the onset of n-pentane condensation. It is also similar to the behavior observed by Pathak et al.[31] during water-nonane co-condensation studies in which highly supersaturated nonane immediately condensed onto the freshly nucleated water particles. PTMs also suggest that CO_2 does not condense onto the particles formed at the highest n-pentane flowrate, Figure 4(f).

B. Particle size (SAXS)

To confirm the interpretation of the PTMs and to determine the parameters of the particle size distribution as the aerosol evolves, we conducted position resolved small angle X-ray scattering (SAXS) measurements. For n-hexane, Figure 5 summarizes the mean particles sizes $\langle r \rangle$ as a function of position, hexane flowrate, and CO_2 concentration. For HF_{C6}, we also show the volume weighted radius, r_V, where

$$r_V = \sqrt[3]{\langle r^3 \rangle} = \langle r \rangle \times \sqrt[3]{\frac{(Z+3)(Z+2)}{(Z+1)^2}} \tag{6}$$

and the radius of gyration, r_G, where

$$r_G = \sqrt{\frac{3\langle r^8 \rangle}{5\langle r^6 \rangle}} = \langle r \rangle \times \sqrt{\frac{3(Z+8)(Z+7)}{5(Z+1)^2}}, \tag{7}$$

$$Z = \left(\frac{\langle r \rangle}{\sigma}\right)^2 - 1, \tag{8}$$

and σ is the width of the size distribution. For a polydisperse aerosol, r_V rather than $\langle r \rangle$ should scale with the density ratio if the mass of particles is conserved. In addition, r_G represents an effective particle size that is independent of the particle shape or structure,[39] and in a polydisperse system, r_G is highly sensitive to the larger particles since as q approaches 0, I_0 is proportional to $\langle r^6 \rangle$. Hence, we can qualitatively explore how the large end of the particle size distribution changes in contrast to the number mean $\langle r \rangle$.
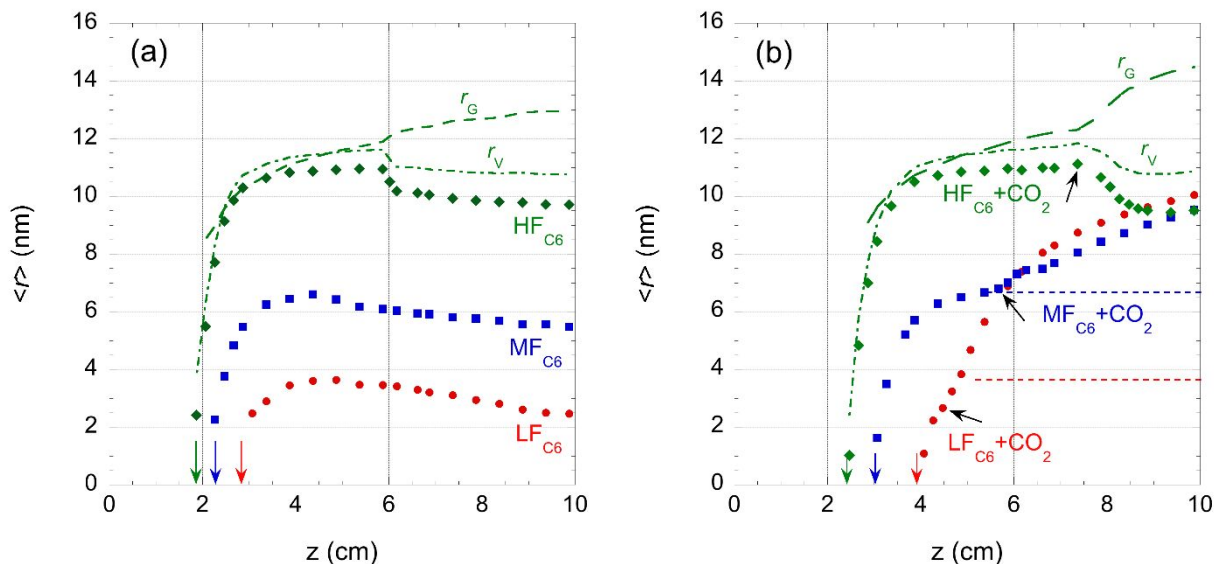
Figure 5. Changes in the mean particle size for (a) pure *n*-hexane and (b) *n*-hexane in the presence of CO_2. For HF_{C6}, values of r_V and r_G, derived from the fit parameters are also illustrated. For MFC6 and LFC6 these are available in Fig. S4. The colored arrows indicate the positions where the temperature difference between T_{PTM} and T_{is} is larger than 1 K for LF_{C6} (red), MF_{C6} (blue), and HF_{C6} (green). The blue and red dotted lines for MF_{C6}+CO_2 and LF_{C6}+CO_2 are the expected average particle size of *n*-hexane if the particles do not freeze and CO_2 does not condense. The black arrows indicate the positions where CO_2 condensation is first observed by FTIR measurements.

Under all experimental conditions, we observe that *n*-hexane particles appear at the same point in the flow as the pressure and temperature suddenly increase. (See Figure 3 for PTMs). In the absence of CO_2, Figure 5(a), $\langle r \rangle$ increases rapidly, reaches a plateau and then decreases again for all hexane flowrates. FTIR measurements (Section III.C) confirm that the size decrease corresponds to the initiation of freezing, i.e. a liquid – crystalline phase transition, and for the MF_{C6} and HF_{C6} cases, the temperature profile (Figure 3(c) and (e)) shows a small, second heat release at the position where the particles shrink. As noted earlier, for LF_{C6}, the second heat release is hard to observe because it is too small given the carrier gas pressure and continued rapid expansion of the flow. At the same time that $\langle r \rangle$ decreases, polydispersity increases rapidly, consistent with a continuous increase in the radius of gyration, r_G, as illustrated for the HF_{C6} experiment.

One challenge these data present – especially at the highest hexane flowrate – is that r_V decreases by more than 5.4 %, corresponding to a volume change of ~17%, i.e. more than can be justified by the ~13 % density increase expected for the *n*-hexane phase transition from bulk liquid to the triclinic solid. Similar excessive changes in mean particle size were observed in our earlier studies with *n*-octane.[28] Furthermore, for the HF_{C6} experiment, the size decrease is extremely sharp occurring in ~6.7 µs, much faster than at lower flow rates or for any other freezing transitions we have observed to date. Nevertheless, as illustrated in Figures S2 for HF_{C6}, the spectra before and after the rapid size change are very well fit assuming that the particles are spheres and follow a Schulz size distribution. This behavior was not a function of the assumed particle size distribution, since fitting the data using a log-normal size distribution (Figure S3 (a))

yielded essentially equivalent $\langle r \rangle$ and polydispersity values. In addition, the value of r_G determined by fitting the low q data directly agrees well with the values determined from the fit parameters, and indicates a rapid appearance of larger structures even as the mean particle size is decreasing (Figure S3(b)).

Although particle coagulation can lead to the formation of larger structures and an increase in r_G, this mechanism cannot explain the simultaneous decrease in $\langle r \rangle$. One way to reconcile the simultaneous decrease in $\langle r \rangle$ or r_V, with the increase in r_G, is to invoke vapor phase transport and the Bergeron process.[40, 41] Here, droplets that freeze first are able to scavenge molecules from the vapor phase more effectively than the remaining liquid droplets because of the difference in vapor pressure between the solid and liquid phases. Thus, the first droplets to freeze can grow while the remaining liquid droplets shrink, thereby broadening the size distribution. In the HF_{C6} experiment, the temperature at the onset of freezing is ~129 K. The corresponding ratio of the liquid to solid equilibrium vapor pressure at this temperatures is ~15.1, where the vapor pressure above liquid n-hexane is calculated using the vapor pressure correlation in Table A-1, and that above solid n-hexane is estimated from the Clausius-Clapeyron equation using the pressure and enthalpy of sublimation at the triple point,[42] 50.8 kJ/mol. Although there appears to be a strong driving force for vapor phase transport, the timescale for this process should also be consistent with the observed ~7 μs characteristic of the rapid change in particle size. In particular, in the free molecular regime, the maximum evaporation rate from a droplet is given by[43]

$$\left.\frac{dr}{dt}\right|_{evap} = -\frac{v}{\sqrt{2\pi m k_B}}\frac{p_e(\langle r \rangle, T_d)}{\sqrt{T_d}} \tag{9}$$

where

$$p_e(\langle r \rangle, T_d) = p_e(T_d)\exp\left(\frac{2v\gamma}{k_B T_d \langle r \rangle}\right), \tag{10}$$

and v is the molecular volume of the condensable, m is the mass of a monomer, k_B is the Boltzmann constant, $p_e(\langle r \rangle, T_d)$ is the equilibrium vapor pressure above a droplet of radius $\langle r \rangle$ and temperature T_d, $p_e(T_d)$ is the equilibrium pressure over a flat surface, and γ is the surface tension of the liquid. For liquid hexane droplets at 129 K, we estimate $\left.dr/dt\right|_{evap} = 3 \times 10^{-7}$ nm/μs. Thus, in 7 μs, droplets should shrink by at most 2.1×10^{-6} nm. If we assume the heat released by freezing rapidly increases T_d until it equals the equilibrium melt temperature T_m = 178 K, the evaporation rate is still only $\left.dr/dt\right|_{evap} = 0.00743$ nm/μs and droplets shrink by 0.05 nm in 7 μs. Our observations that evaporation from n-alkane droplets under our experimental conditions is negligible, agrees with the n-nonane particle growth study of Pathak et al.[43] They found that even during rapid condensational growth, the evaporation rate of n-nonane was negligible despite droplet temperatures estimated to be ~10 K above T_m. In the real experiment, evaporation should be even slower because the droplets are not in a vacuum; heat transfer to the carrier gas will remove energy from the freezing droplets and vapor molecules can recondense. Thus, evaporation alone appears to be too slow to decrease the droplet size in the time available.

An alternative way for the average particles size to decrease is particle shattering. Wildeman el al.[44] and others[45, 46] have observed that water droplets can shatter when freezing starts at the

surface and proceeds inward. For water, this process is driven by decreased density of the ice relative to that of the liquid, and, thus, as the droplet freezes the pressure of the remaining liquid increases. Once the pressure inside the droplet exceeds the tensile strength of the ice shell, the shell cracks open, and the droplet can explode. The presence of gases initially dissolved in the liquid can also play a role this process.[46] From their model calculations, however, Wildeman et al.[44] concluded that water droplets with radii smaller than ~50 μm remain intact because the surface energy dominates and droplet explosion becomes implausible. Although normal alkanes are known to exhibit surface freezing,[28, 29, 47, 48] shattering is unlikely because n-alkanes densify on freezing. Furthermore, the bulk mechanical properties of the n-alkanes are not that different from those of water to allow droplets in our size range to shatter. This picture could, potentially, change if freezing occurs in the presence of dissolved gases or if the layered structure of the frozen alkanes weakens the nanodroplets in a way not captured by the bulk properties. A full understanding of the complex processes reshaping the aerosol size distribution upon freezing, that should also include the possibility of dissolved gases and particle shattering, requires a level of modeling that is beyond the scope of the current work.

In Figure 5(b), the change in particle size for $HF_{C6}+CO_2$ mirrors that observed for HF_{C6}, and rapid decreases in $\langle r \rangle$ and r_V are again accompanied by a second heat addition (Figure 3(f)). The discrepancies between $\langle r \rangle$, r_V, and r_G are even more pronounced than in the HF_{C6} case, and it is difficult to decide whether particles simply froze, or froze and shattered, where the latter could be aided by dissolved CO_2 being expelled from the growing crystal.[46] Indications that CO_2 could be condensing under these conditions include a very slight increase in $\langle r \rangle$ and r_V near the nozzle exit, a more rapid increase in r_G relative to the pure n-hexane case that is consistent with CO_2 condensation onto the largest particles, and a slightly less good fit to the SAXS data near $q \sim 0.5$ A^{-1} (Figure S2(b)). The absolute scattering intensities of the SAXS spectra after the size "jump" are also higher than in the absence of CO_2, especially at low q, consistent with a higher scattering length density for solid CO_2 (1.36×10^{-5} A^{-2}) than solid n-hexane (8.87×10^{-6} A^{-2}). Attempts to improve the fit near $q \sim 0.5$ A^{-1}, by using other shapes or particle structures, including ellipsoidal and core-shell structure models, were not successful. In the future, MD simulations could provide additional molecular level insight into the partitioning of CO_2 between the vapor and condensed states under these conditions. Finally, as discussed in more detail in Section III.C.2, FTIR measurements show that CO_2 condenses at the same point in the flow that $\langle r \rangle$ decreases and r_G increases (black arrow in Figure 5(b)).

Interpreting the $LF_{C6}+CO_2$ and $MF_{C6}+CO_2$ experiments is more straightforward. The large increase in particle size in the presence of CO_2 is clear evidence for CO_2 condensation. In the case of $MF_{C6}+CO_2$, the second growth phase is clearly separated from the first, and the dashed line in Figure 5(b) corresponds to the expected $\langle r \rangle$ for n-hexane particles prior to freezing in the absence of CO_2. The FTIR measurements (Section III.C.2) confirm the size measurements since the first position where we observe condensed CO_2 (black arrow in Figure 5 (b)) corresponds to particle sizes slightly larger than the expected size of unary n-hexane particles. This situation mirrors the experiments of Tanimura et al.[23] where water ice particles formed well upstream of CO_2 heterogeneous nucleation. In $LF_{C6}+CO_2$, CO_2 starts to condense just before n-hexane condensation stops. The FTIR measurements also show that CO_2 condensation does not strongly affect the condensation rate of n-hexane. Thus, in the $LF_{C6}+CO_2$ experiment particle formation is initiated by homogeneous nucleation and growth of n-hexane, followed by simultaneous

condensation of *n*-hexane and CO_2 until most of the *n*-hexane vapor condenses, and finally continued growth via pure CO_2 condensation.
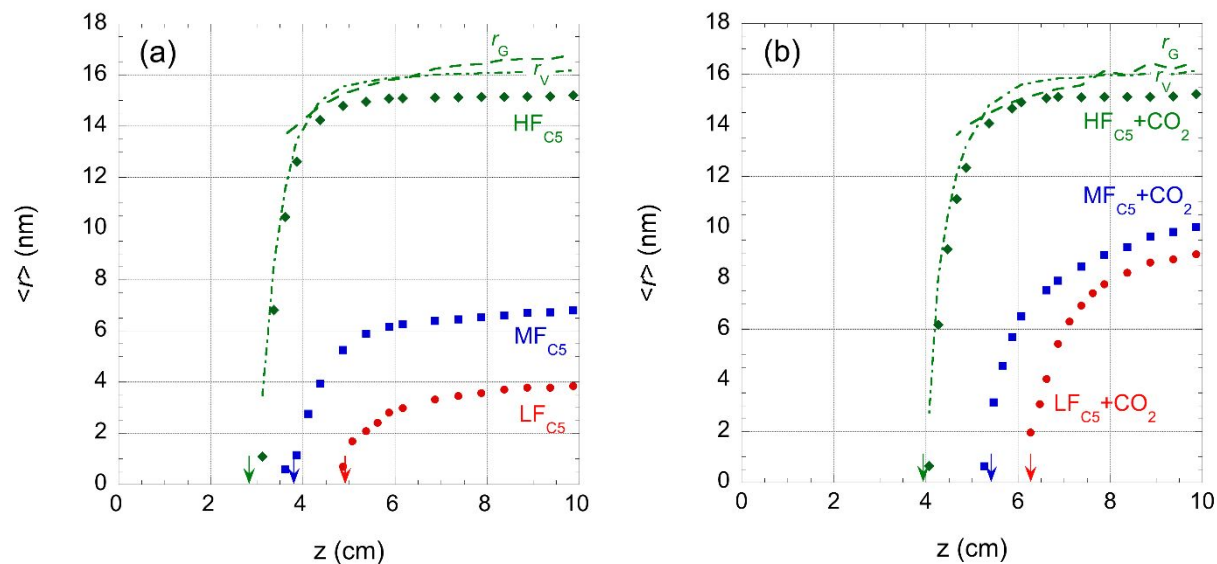
Figure 6. Changes in the mean particle size for (a) pure *n*-pentane and (b) *n*-pentane in the presence of CO_2. For HF_{C5}, values of r_V and r_G, derived from the fit parameters are also illustrated. For MF_{C5} and LF_{C5} these are available in Fig. S5. The colored arrows indicate the positions where the temperature difference between T_{PTM} and T_{is} is larger than 1 K for LF_{C5} (red), MF_{C5} (blue), and HF_{C5} (green).

Figure 6 illustrates the particle sizes measured for *n*-pentane in the absence and presence of CO_2. There is no evidence for freezing of the *n*-pentane droplets under any conditions. For HF_{C5} and $HF_{C5}+CO_2$, the SAXS spectra near the exit are well fit assuming spherical particles (Figure S2(c)). Once the aerosol has stopped growing, the particle sizes are essentially the same, r_V and r_G do not deviate much from the trajectory of $\langle r \rangle$ and the absolute scattering intensities of HF_{C5} and $HF_{C5}+CO_2$ are very close to each other. These observations all support the interpretation that at the highest *n*-pentane flow rate the droplets do not freeze and CO_2 does not condense. In contrast, at the two lower flow rate conditions, $LF_{C5}+CO_2$ and $MF_{C5}+CO_2$, particles grow smoothly to much larger sizes when CO_2 is present than when it is absent. Thus, the size data are consistent with the increased heat release observed in Figures 4(b) and 4(d) and our earlier interpretation that CO_2 condenses onto the *n*-pentane droplets as soon as they are formed.

Since the SAXS data also yield estimates for the aerosol number densities, we calculated the vapor-liquid nucleation rates for the pure alkanes, and where possible, for the pure alkanes in the presence of CO_2. The results are summarized in Table 2 and illustrated in Figure A2. Where possible, we evaluated the rates both shortly after the onset of condensation and at the same fixed location (7 cm downstream of the throat) used in Ogunronbi's et al.'s work.[32] In all cases the nucleation rates at comparable alkane partial pressure in the presence or absence of CO_2 agree

within a factor of two as do the nucleation rates based on number densities measured at the two different locations.

C. Alkane Phase and CO_2 condensation via FTIR

Although PTMs and SAXS data provide a relatively consistent picture of particle formation and aerosol evolution, FTIR spectroscopy can provide additional, independent data regarding the state of each condensable species. Ideally, FTIR can also determine the overall composition of the aerosol and lead to more accurate data analysis. Here, we present the FTIR data, used to test the conclusions from the joint PTM + SAXS analysis that
  1) *n*-hexane particles freeze,
  2) *n*-pentane particles do not freeze,
  3) CO_2 heterogeneous nucleation occurs in all cases except $HF_{C5}+CO_2$.

C.1 Alkane condensation and freezing

As detailed in the work of Pathak et al.[31] and Modak et al.[28, 29] changes in the total absorbance in the C–H vibrational stretching region (2800 – 3050 cm^{-1}) can be used to follow the changes in the distribution of alkanes between the vapor, liquid, and solid states as the alkane condenses and the droplet freeze in the supersonic nozzle.

Figure 7 compares selected IR spectra for HF_{C6} and $HF_{C6}+CO_2$ at comparable degrees of condensation. Prior to the "jump" in the particle size (Figure 7(a) and (b)), the spectral shapes, with and without CO_2, are almost identical. Discrepancies appear immediately after the jump, Figure 7(c) and (d), where all the peaks in HF_{C6} are shifted to lower wavenumber whereas the peaks in $HF_{C6}+CO_2$ do not change. More pronouncedly, the antisymmetric CH_3 stretching band at around 2956 cm^{-1} splits only in the absence of CO_2. The split of the antisymmetric methyl stretching band is associated with the dipole moment parallel and perpendicular to the skeletal plane in the triclinic structure of solid phase *n*-alkanes: The band at 2953 cm^{-1} is parallel and the band at 2962 cm^{-1} is perpendicular to the skeletal plane.[49] These changes in spectral feature after the jump at HF_{C6} are evidence for freezing of *n*-alkane. Similar behavior is observed for the lower *n*-hexane flowrates (Figures S6): in the absence of CO_2, the antisymmetric methyl stretching band splits when the particle size starts to decrease, whereas with CO_2, there are no changes in the *n*-hexane IR spectra up to the exit of the nozzle.
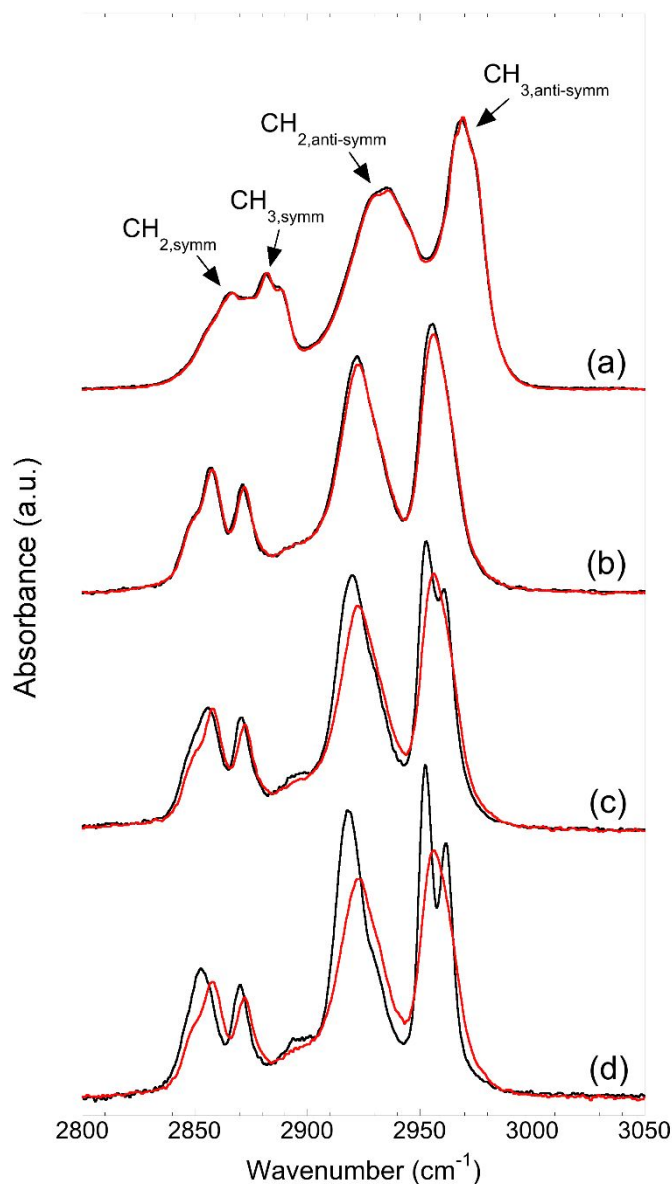
Figure 7. Total absorbance in the CH stretch region of the IR spectrum for HF_{C6} (black) and $HF_{C6}+CO_2$ (red) at comparable degrees of alkane condensation. Spectra were baseline corrected and adjusted for the density of the flow but not scaled otherwise. (a) Spectra measured prior to particle formation are those of the pure vapor (HF_{C6}: at 1.27 cm, $HF_{C6}+CO_2$: at 1.67 cm). The anti-symmetric and symmetric stretching vibration bands of CH_2 and CH_3 are indicated. (b) Just before the sharp particle size decrease (HF_{C6}: at 5.87 cm, $HF_{C6}+CO_2$: at 7.37 cm), the spectra contain contributions from the vapor and the liquid. (c) Immediately after the sharp particle size decrease (HF_{C6}: at 6.17 cm, $HF_{C6}+CO_2$: at 8.87 cm) and (d) at the exit of the nozzle (HF_{C6}: at 9.87 cm, $HF_{C6}+CO_2$: at 9.87 cm), the presence of the solid is only detected in the pure alkane case.

Particles do not appear to crystallize in the presence of CO_2 at any of the *n*-hexane flowrates. One possible explanation is that *n*-hexane crystallization is hindered by CO_2 dissolved within the particles. The presence of this species could easily lower the crystallization temperature as it would naturally lower the melt temperature. Alternatively, even if the alkane solidifies, the CO_2 molecules within the particles could prevent the crystal organization required to generate the peak splitting.

Recently, Qiu and Molinero[50] investigated the crystal nucleation mechanism of *n*-alkanes in the presence of an interface. They showed that alkanes prefer to align perpendicular to the alkane-vacuum interface, but can align parallel to an alkane-fluid interface if the strength of the attractions between alkane and fluid are strong enough. At an alkane-vacuum interface, the crystal nucleus first forms as a perpendicularly aligned bundle of *n*-alkane molecules at the interface that then drives surface freezing, followed by heterogeneous crystal nucleation of the remaining fluid. In contrast, when the alkane interacts more strongly with the fluid molecules at the interface, the alkane configurations at the surface reflect those in the bulk, and crystal nucleation is more likely to start homogeneously throughout the liquid. Thus, if CO_2 adsorbs to the alkane droplet interface and interacts strongly enough with hexane to prevent surface freezing, it may be more difficult for *n*-hexane particles to crystallize. Either way, the fact that hexane does not appear to freeze is surprising, especially for the $HF_{C6}+CO_2$ experiment, because the temperature increases at the size jump are comparable or slightly larger than in the HF_{C6} experiment. Furthermore, the absence of crystallization makes it even more difficult to understand the rapid decrease in the mean particle size observed in the $HF_{C6}+CO_2$ experiment.

The total IR absorbance of the *n*-pentane at the nozzle exit with and without CO_2, Figure 8, confirms that *n*-pentane particles never crystallize within the nozzle. This result is consistent with those from PTM and SAXS. Despite temperature differences of ~40 K at the exit of the nozzle between LF_{C5} and $LF_{C5}+CO_2$ (see Figures 4(a), 4(b)), and ~30K between MF_{C5} and $MF_{C5}+CO_2$ (see Figures 4(c), 4(d)), the IR spectra overlap nicely, confirming our assumption that the liquid spectra are not very temperature dependent.
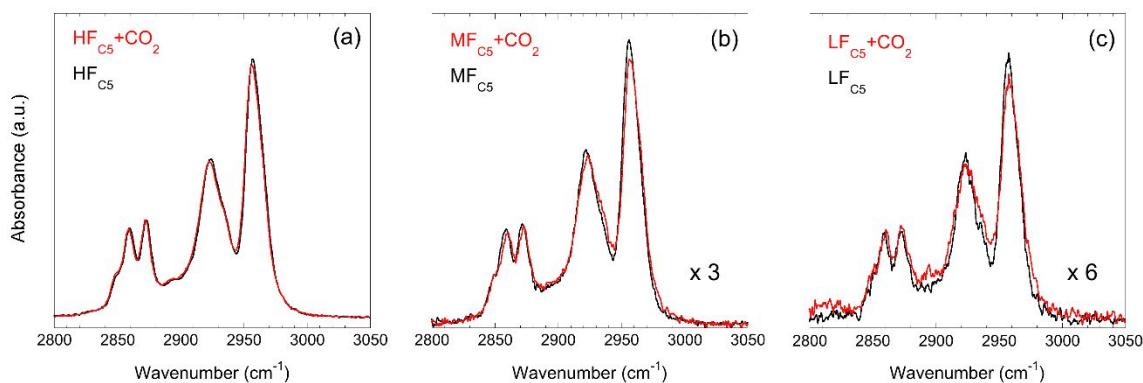
Figure 8. Total absorbance of (a) HF_{C5} (black) and $HF_{C5}+CO_2$ (red), (b) MF_{C5} (black) and $MF_{C5}+CO_2$ (red), and (c) LF_{C5} (black) and $LF_{C5}+CO_2$ (red) near the exit of the nozzle. Spectra were baseline corrected and adjusted for density of the flow.

C.2 CO$_2$ Deposition

CO$_2$ condensation can also be monitored directly by observing changes in the antisymmetric stretching vibration. As illustrated in Figure 9(a), prior to any condensation, the normalized absorptivity of CO$_2$ is highly consistent between the experiments. Furthermore, as detailed in Section II.D and illustrated in Figure 9(b), the gas phase absorbance spectra can be predicted quantitatively using a spectral calculator (SpectralCalc.com) based on HITRAN data, and modeling the experiment as two gas cells (room air + nozzle) in series.
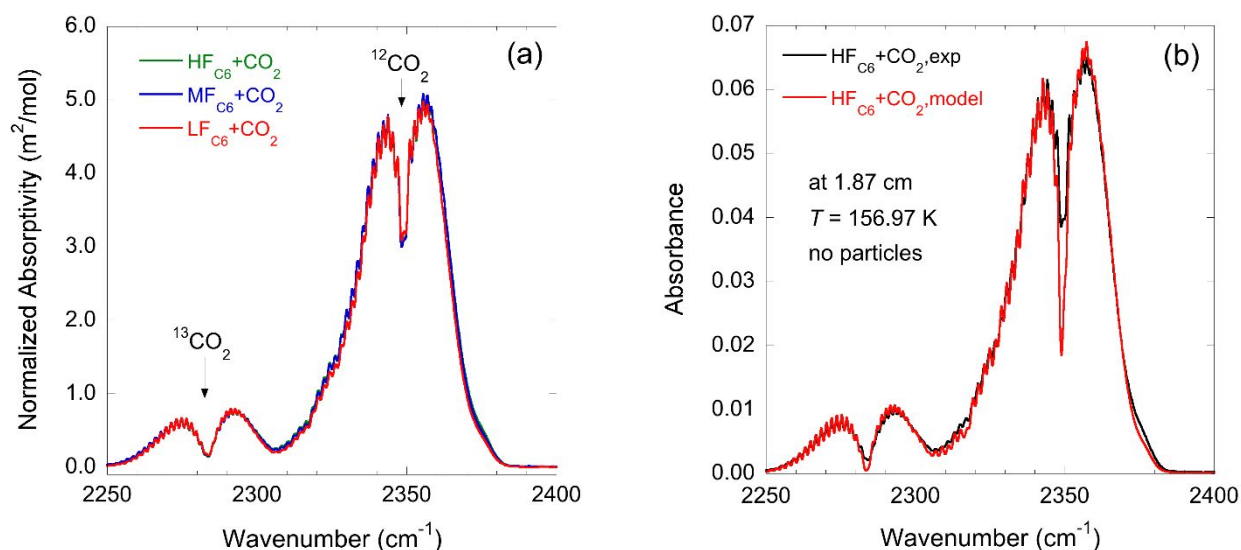
Figure 9. Prior to condensation, gas phase CO$_2$ spectra agree (a) with each other and (b) with the predictions of simple model of the experiment. Experimental spectra were baseline corrected and in (b) shifted by +0.5 cm^{-1} for better agreement with the model.

For crystalline CO$_2$, the intensity and structure of these bands is very sensitive to the size, shape and structure of the CO$_2$ domains.[35-37, 51-62] Although it is possible to gain insight into the structure of the binary particles by comparing the spectra to predictions available in the literature, that is the subject of a separate publication. Here, we only use changes in the CO$_2$ spectra to identify if and when CO$_2$ condenses.

Figures 9(b) and 10 illustrate the results of the HF$_{C6}$+CO$_2$ experiment where PTM and SAXS results gave only indirect evidence that CO$_2$ might be condensing. In particular, PTM suggested a higher second heat addition, and SAXS indicated a more rapid increase in r_G compared to the pure hexane case. Initially (Figure 9(b)), the experimental spectrum and modeled CO$_2$ gas absorption curve are in almost perfect agreement. Even as n-hexane particles are formed, the experimental and predicted gas phase CO$_2$ absorbances continue to agree (Figure 10(a) and 10(b)), and the systematic decrease in absorbance is consistent with the decrease in density of the expanding flow. Finally, in Figure 10(c), right after $\langle r \rangle$ starts to decrease rapidly, the experimental spectrum deviates significantly from the predicted gas phase spectrum. In

particular, the shape and intensity of the experimental peaks centered at 2345.5 cm^{-1} and 2360.5 cm^{-1} differ distinctly from those predicted for gas phase CO_2. We interpret this as the signature for CO_2 condensation. As noted earlier, the contradictory behavior – CO_2 condensation from FTIR and a decrease in $\langle r \rangle$ from SAXS – suggests that CO_2 selectively condenses only onto the larger *n*-hexane particles. Similar behavior, i.e. initial agreement between the experimental and predicted gas phase CO_2 spectra followed by a sudden and dramatic change in the shape of the experimental spectra, was observed in the other experiments where CO_2 condensed.
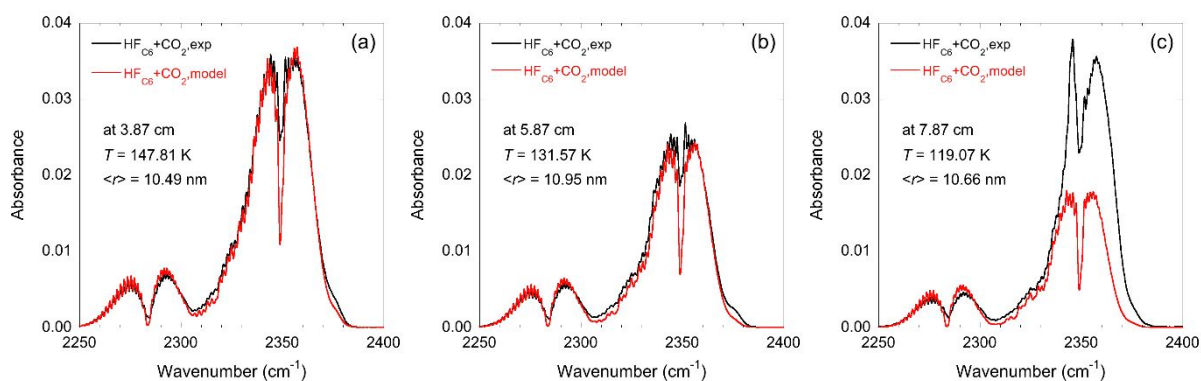
Figure 10. The predicted CO_2 and measured adsorption spectra agree reasonably well (a,b) until CO_2 condensation starts (c). The steady decrease in the predicted CO_2 adsorption is largely a function of the density of the gas.

Given the good agreement between the model and the experiments prior to CO_2 condensation, we calculated the ratio of the areas under the experimental and predicted absorbance curves A_{exp}/A_{pred}. As illustrated in Figure 11, when CO_2 is solely in the vapor phase this ratio is very close to 1, increasing rapidly when CO_2 starts to condense. As expected, CO_2 does not condense in the HF_{C5} case. If we use the criterion that we can detect CO_2 condensation once A_{exp}/A_{pred} > 1.3, then the positions where $A_{exp}/A_{pred} = 1.3$ correspond to the black arrows in Figure 5 and 6. Conversely, the arrows in Figure 11 correspond to our current definition of the "onset of heterogeneous CO_2 condensation" i.e. the locations where $S_{CO2,ice}$ reaches its maximum.
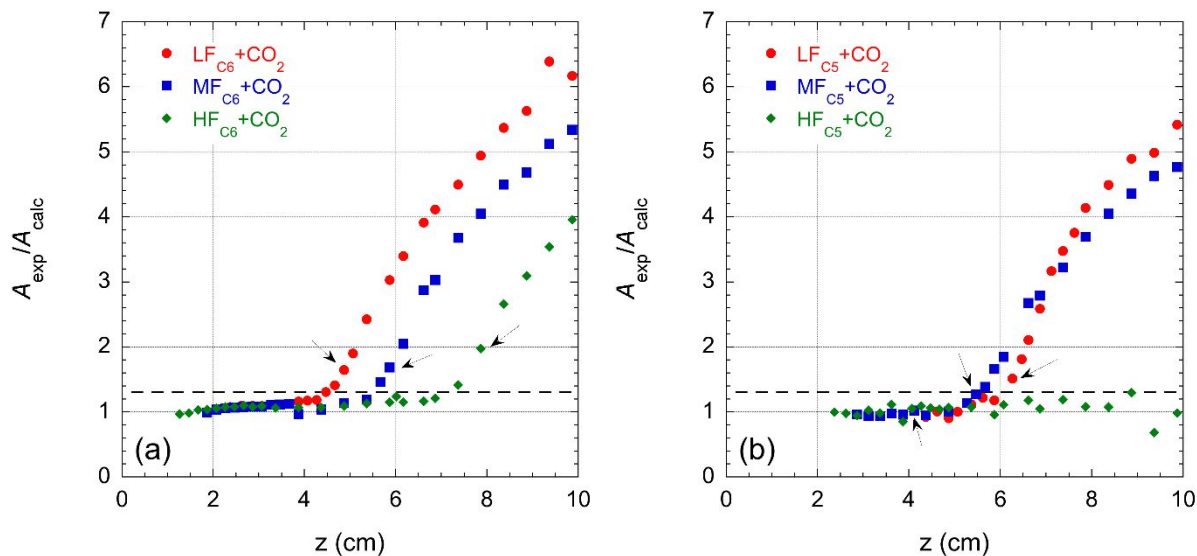
Figure 11: The ratio A_{exp}/A_{pred} provides a convenient way to accurately locate the onset of CO_2 condensation onto the (a) *n*-hexane (b) *n*-pentane particles. Black arrows indicate the location of the maximum saturation reached by CO_2 in the experiment, $S_{CO2,ice}$.

D. Further discussion

The key motivations for this work was to examine whether differences in seed particle composition and phase significantly affect heterogeneous nucleation of CO_2 from the vapor phase and to explore the mechanism of CO_2 heterogeneous nucleation on the microsecond timescale. A precondition for heterogeneous nucleation is, of course, the presence of particles, and, as discussed in more detail below, in some of the *n*-pentane experiments it is the formation of seed particles that controls when CO_2 nucleates heterogeneously rather than the supersaturation of the CO_2.

We begin by comparing the current *n*-alkane+CO_2 results to the ice+CO_2 results of Tanimura et al.[23] and the recent data for CO_2 heterogeneous nucleation onto iron oxide and silica nanoparticles by Nachbar et al.[63] in Figure 12. The conditions corresponding to the onset of CO_2 heterogeneous nucleation are shown in terms of $S_{CO2,ice} = p_{CO2}/p^e_{CO2,s}(T)$ and temperature, where $p^e_{CO2,s}(T)$ is the equilibrium vapor pressure of solid CO_2. We note that Tanimura et al. originally defined onset as the conditions present when they first detected heat release due to CO_2 condensation. Here we define onset as the maximum $S_{CO2,ice}$ reached in the expansion. The latter definition is more convenient because it is straightforward to calculate from the position resolved values of p_{CO2} and T available from the integrated data analysis. Furthermore, unlike the heat release approach the maximum $S_{CO2,ice}$ value does not depend on any fitting procedures and is less dependent on process variables like carrier gas pressure or CO_2 concentration. It is also consistent with the "onset" definition used in our homogeneous nucleation studies and, finally, it is still well defined when CO_2 condensation occurs essentially simultaneously with seed particle growth. For consistency, we reanalyzed the data of Tanimura et al. – using his position resolved

data and the current definition of onset – and include these in the figure as well. Finally, we include the homogeneous nucleation onset data of Duff,[33] extrapolated into our temperature regime, since homogeneous nucleation of CO_2 is the natural upper limit for these heterogeneous nucleation experiments. Recent measurements[64] confirm that this extrapolation is robust.
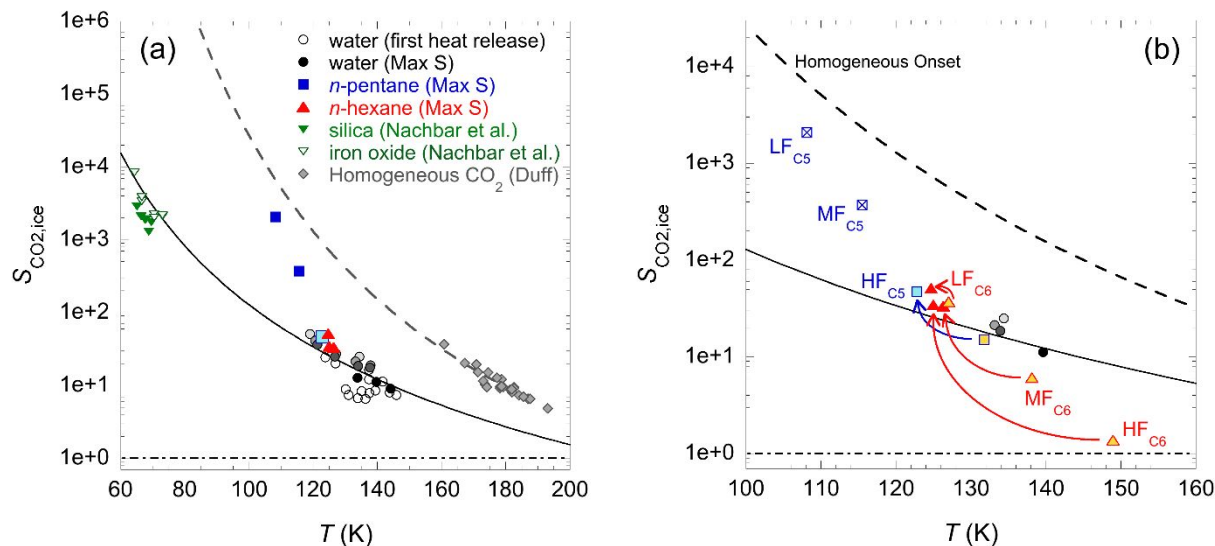
Figure 12. The conditions at the onset of heterogeneous and homogeneous nucleation of CO_2. The solid black line corresponds to the extrapolated vapor-liquid equilibrium line for CO_2 and the dashed grey line is the extrapolation of Duff's[33] onset conditions for homogeneous condensation. (a) The circles are the heterogeneous nucleation onset conditions on solid water particles by Tanimura et al.[23]: Open circles correspond to the first detected heat release, and filled circles correspond to the maximum supersaturation reached in the experiment. The grayscale used for the filled circles indicates the size of the seed particles and varies from light gray ($r_G \approx 2$ nm) to black ($r_G \approx 4$ nm). Dark blue squares are the conditions at the maximum supersaturations reached in n-pentane+CO_2 and here n-pentane particle formation controls heterogeneous nucleation. The light blue square is the condition at the exit of the nozzle in HF_{C5}+CO_2, where the temperature for HF_{C5}+CO_2 at the exit is calculated based on the assumption there is no CO_2 condensation. Red solid triangles are the conditions at the maximum supersaturations reached in the n-hexane+CO_2 experiments where the temperatures have been adjusted by the amounts corresponding to the equivalent n-hexane experiments without CO_2 (LF_{C6}+CO_2: +1.5 K, MF_{C6}+CO_2: +3 K, HF_{C6}+CO_2: +6 K). The onset conditions on silica and iron oxide particles (upside-down triangles) are from Nachbar et al.[63] The onset conditions for homogeneous nucleation (diamonds) are from Duff.[33] (b) Enlarged from (a) for heterogeneous nucleation of CO_2 on water ice, n-pentane, and n-hexane particles. The selected data points for the water ice particles (circles, same gray scales as in (a)) correspond to an inlet CO_2 mole fraction of 0.145 which is the closest condition to the current work, y_0~0.12. The initial $S_{CO2,ice}$ values correspond to those of the gas phase where the seed particles were formed (yellow square: HF_{C5}+CO_2, yellow triangles: n-hexane+CO_2) and the lines with arrows join the initial and maximum values of $S_{CO2,ice}$ but do not follow the experimental $S_{CO2,ice}$–T path. The n-alkane seed particles are labeled near each symbol in the figure, but "+CO_2" labels are omitted. For LF_{C5}+CO_2 and MF_{C5}+CO_2 (squared ×) the initial and maximum $S_{CO2,ice}$ values coincide.

A striking feature of Figure 12 is the degree of saturation with respect to the solid CO_2 that is required to initiate heterogeneous CO_2 nucleation irrespective of the seed particle composition, i.e. water ice, n-hexane, n-pentane, iron oxide or silica. Nevertheless, since all of the conditions measured here are still well below the extrapolated onset conditions for homogeneous CO_2 nucleation, the latter process is highly unlikely. In Figure 12(a), Tanimura et al.'s data based on heat release lie below the saturation line of liquid CO_2, whereas those corresponding to the maximum supersaturation follow the saturation line of liquid CO_2 quite closely. The radii of the water ice particles are indicated with a gray scale ranging from light gray, 2.1 – 2.3 nm, mid-gray, 3.0 – 3.2 nm, dark-gray, 3.6 – 3.7 nm, and black, 4.1 – 4.3 nm. The smallest seed particles are located slightly above the saturation line of liquid CO_2, while the largest seed particles are located slightly below the saturation line. In Figure 12(b), only the onset conditions with an inlet CO_2 mole fraction of 0.145 are selected to show the trend more clearly. This trend confirms the expectation, based on classical heterogeneous nucleation theory, that as the size of the seed particle increases, lower supersaturations are required to initiate heterogeneous nucleation. Nachbar et al.[63] observed the same trend for heterogeneous nucleation of CO_2 on silica (solid upside-down triangles) and iron oxide (open upside-down triangles) particles. In their experiments, they determined that the contact parameter was the same for both particle types, and the change in onset conditions directly reflects the change in particle size: the silica particles were larger (2.44 – 3.04 nm) than the iron oxide particles (1.89 – 2.13 nm). The $S_{CO2,ice}$ values required for heterogeneous nucleation of CO_2 on n-hexane particles, marked with red triangles in Figure 12(a), are comparable to those required to nucleate onto water ice particles at similar temperatures. However, the largest n-hexane particles, ~11 nm, is about 5 times larger than the smallest water particles, 2.1 nm.

According to Fletcher's heterogeneous nucleation theory,[24] the rate of heterogeneous nucleation on a spherical particle depends both on the size and surface properties of the seed particle. When the particle radius is less than 100 nm, rates increase rapidly with size and, therefore, a decrease in rate with an increase in size suggests that the surface properties of n-hexane particles increase the barrier to heterogeneous nucleation of CO_2 relative to water ice. One of the most important surface properties is the contact angle, that is a measure of the intermolecular forces acting between the surface and nucleating material. Mahata et al.,[65] for example, showed that on a series of different flat substrates, increasing the contact angle between water and the substrate from 5° to 102.5° increased the critical supersaturation for heterogeneous nucleation of the liquid from 0.66 to 25. Thus, within the framework of classical heterogeneous nucleation theory, the contact angle between the n-hexane and CO_2 should be larger than the contact angles between ice, silica or iron oxide and CO_2. The problem here is that n-alkanes wet most surfaces very well so it is difficult to imagine that liquid alkanes would not wet CO_2.

Another big difference between n-hexane seed particles and ice, silica, or iron oxide particles is their state. While the latter three are clearly solids, n-hexane did not appear to crystallize in the presence of CO_2. As discussed earlier, the possible reasons for this include adsorbed or dissolved CO_2 inhibiting surface and/or bulk freezing. Nevertheless, we also found that CO_2 condensation onto n-hexane particles started at temperatures (124.7 – 126.3 K) that are very close to the those where pure n-hexane particles begin to freeze (122.9 – 128.5 K). This may imply that CO_2 only starts to nucleate heterogeneously on n-hexane particles when the latter can provide a solid enough surface. This observation is consistent with the $S_{CO2,ice}$ trajectory for $LF_{C6}+CO_2$ in Figure

12(b). While the $S_{CO2,ice}$ values for $MF_{C6}+CO_2$ and $HF_{C6}+CO_2$ start from well below the extrapolated liquid equilibrium line, the $S_{CO2,ice}$ for $LF_{C6}+CO_2$ is already above the onset $S_{CO2,ice}$ values of the other conditions when n-hexane particles are initially formed. However, CO_2 does not start condensing onto n-hexane particles at $LF_{C6}+CO_2$ until it reaches a lower temperature where the n-hexane particles may start to solidify. Even though n-hexane particles did not appear to crystallize to the usual triclinic structure in the presence of CO_2, they could be viscous enough or in an amorphous or glassy state when they are this highly supercooled. Thus, the reason why the supersaturations required for CO_2 to condense on large n-hexane particles are comparable to or higher than smaller water particles, may be that CO_2 can only condense after the n-hexane particles are solid enough. Similar behavior has been discussed in the atmospheric water ice nucleation literature where water ice will only nucleate heterogeneously onto organic aerosols when they are glassy.[4, 66, 67]

In the heterogeneous water ice nucleation literature,[3] the initiation of ice nucleation near the extrapolated vapor-liquid line is often interpreted as an indication that condensation of the supersaturated liquid precedes the heterogeneous nucleation of ice. Although this is an intriguing possibility, we do not have a reference spectrum for liquid CO_2 that we could use to examine whether our spectra are consistent with this idea.

For n-pentane, the maximum supersaturations required for CO_2 to nucleate under LF and MF conditions appears to be much larger than those required to nucleate onto n-hexane or water particles. In a sense, Figure 12(a) is misleading because it does not show the conditions under which the alkane particles first form. In fact, the very large saturations required to initiate CO_2 condensation at LF and MF correspond to the conditions present when the seeds started to form. In contrast, particles under HF condition form and grow to $\langle r \rangle \approx$ 15 nm at temperatures and $S_{CO2,ice}$ values below the extrapolated CO_2 v-l equilibrium line. Figure 12(b) shows the values of $S_{CO2,ice}$ where the largest n-pentane particles form (yellow square) and the conditions at the exit of the nozzle (light blue square). As shown in the figure, CO_2 does not nucleate onto the particles even though the supersaturation at the exit of the nozzle in $HF_{C5}+CO_2$ appears to be high enough for CO_2 to start condensing.

A possible reason that CO_2 does not condense onto the large n-pentane particles in the $HF_{C5}+CO_2$ experiment may be that these particles are still in the liquid state. If the n-pentane easily wets the developing CO_2 critical cluster, it may be impossible for the cluster to grow, thereby inhibiting the phase transition. This scenario is indirectly supported by the observation that CO_2 condensation only proceeds on the large n-hexane particles when temperatures are close to the freezing point observed for the pure droplets. Thus, solidification into an amorphous or glassy state may be an important first step for heterogeneous nucleation to proceed in these systems. In the $MF_{C5}+CO_2$ and $LF_{C5}+CO_2$ cases, the high $S_{CO2,ice}$ may drive heterogeneous nucleation under conditions where there is not yet enough alkane in the seed particle to effectively suppress nucleation by wetting.

The heterogeneous nucleation of a liquid onto a liquid or soft surface has been addressed in the literature, and in this scenario nucleation rates increase relative to heterogeneous nucleation of the same liquid onto a solid or rigid surface.[68-70] To our knowledge heterogeneous nucleation of a solid onto a liquid surface has not been discussed and our experiments may be the first to explore this regime. Further studies, in particular MD simulations, could lead to better molecular level explanations of the wide range of heterogeneous nucleation behavior observed in these studies.

IV.   Summary and Conclusions

We extended the earlier heterogeneous nucleation studies of CO_2 onto water ice particles, by changing the seed particles in order to explore the effects of particle size, physical state and composition on heterogeneous nucleation. Two n-alkanes, n-hexane and n-pentane were chosen as materials to make larger seed particles with different condensed states via homogeneous nucleation in a supersonic nozzle. PTM, SAXS, and FTIR measurements characterized the evolution and state of both unary and binary particles. For n-hexane alone, liquid particles form and subsequently freeze, whereas for n-pentane alone, freezing does not occur within the timescale of our experiments. When CO_2 is present in the flow, the PTM shows two distinct temperature increases for all conditions of n-hexane+CO_2. Combined with particle size information obtained from SAXS, it is clear CO_2 condenses onto n-hexane particles in the LF_{C6}+CO_2 and MF_{C6}+CO_2 experiments since particles are much larger compared than those formed in the absence of CO_2. In the case of HF_{C6}+CO_2, the particle size profile is very similar to the HF_{C6} case: $\langle r \rangle$ increases rapidly, reaches a plateau, and then exhibits a sudden decrease that is larger than expected from the expected change in density upon freezing. Nevertheless, FTIR measurements show conclusive evidence for condensation of CO_2 in the HF_{C6}+CO_2 experiment, whereas the characteristic change in the C–H stretch region associated with solid n-hexane is never observed in the presence of CO_2. Full crystallization of n-hexane could be hindered by a small amount of CO_2 dissolved in the droplets, or by suppression of surface initiated freezing. Interpreting the n-pentane+CO_2 cases is more straightforward. From PTM and SAXS data, one smooth step in temperature and size increase in LF_{C5}+CO_2 and MF_{C5}+CO_2 shows n-pentane and CO_2 condense simultaneously as soon as n-pentane forms small clusters, and neither technique shows evidence of CO_2 condensation in HF_{C5}+CO_2. FTIR results agree with the observations of PTM and SAXS in all cases.

The onset data of heterogeneous nucleation of CO_2 on n-alkane particles was compared to both homogeneous nucleation of CO_2 and heterogeneous nucleation of CO_2 on water ice, silica and iron oxide particles. In all cases, it is clear that CO_2 condensation proceeds heterogeneously since the supersaturation required is far less than that required to initiate homogeneous nucleation of CO_2. In the n-pentane+CO_2 cases, the maximum supersaturation required is large, and approaches the extrapolated onset supersaturation of homogeneous nucleation because these are the conditions under which n-pentane particles first emerge. The onset conditions for n-hexane+CO_2 suggest that the molecular interactions between CO_2 vapor molecules and n-hexane surface are less favorable to that between CO_2 vapor molecules and water ice surface since the supersaturations required for CO_2 condensation are comparable when the n-hexane particles are significantly larger than the water ice particles. There are two possible reasons for the less favorable molecular interactions at the interface: a larger contact angle or the presence of a liquid surface. The data could imply that the contact angle between CO_2 nucleus and n-hexane particle is larger than that between CO_2 nucleus and water ice particle, or, it could simply mean that it is much difficult to make a solid CO_2 nucleus on a liquid surface than on a solid surface. The temperature that CO_2 starts to condense is very close to the freezing temperature of n-hexane particles, suggesting that n-hexane particle may be in an amorphous solid phase and CO_2 can start condense on a solid surface. This may also be why CO_2 does not condense on the largest n-pentane particles in HF_{C5}+CO_2, that is CO_2 does not condense on the n-pentane particles because they are still liquid. The mechanism of heterogeneous nucleation of CO_2, in these unusual cases, is still unclear and should be investigated by direct simulations.

Appendix
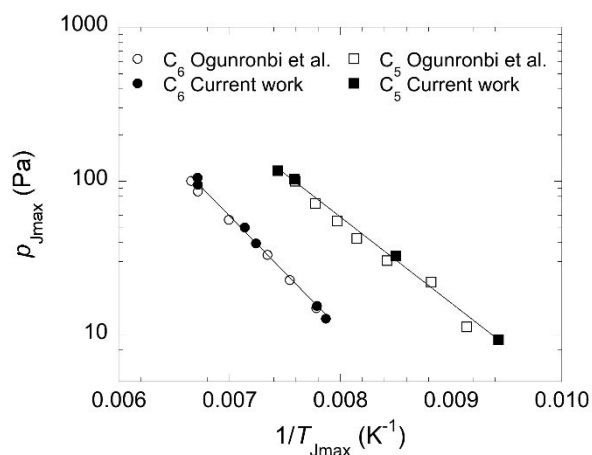
Figure A-1. The (p_{Jmax}, T_{Jmax}) values determined for *n*-pentane and *n*-hexane in the current work are in good agreement with those of Ogunronbi et al.[32] Both data sets follow the expected linear behavior when $\log p_{Jmax}$ is plotted as a function of $1/T_{Jmax}$. The presence of CO_2 and the higher carrier gas pressure do not appear to affect the nucleation process.
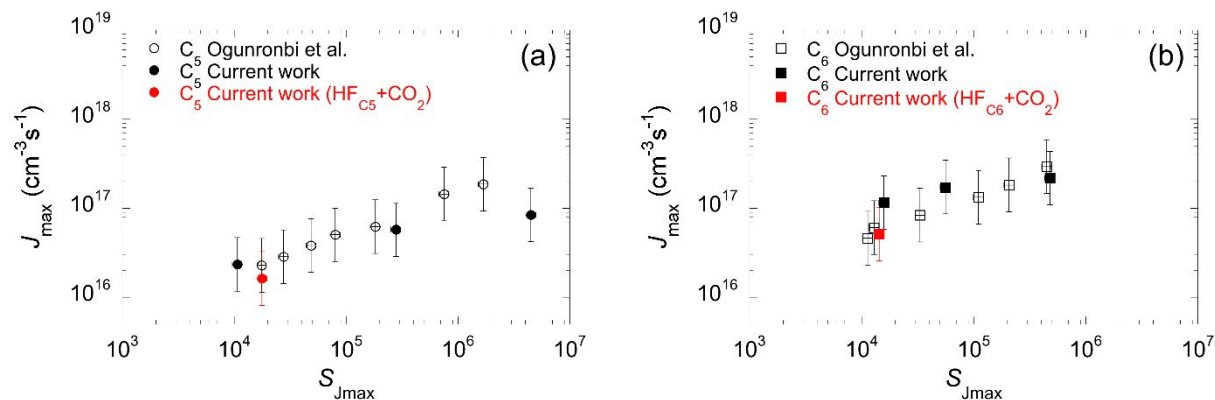
Figure A-2. The maximum nucleation rates measured for (a) *n*-pentane and (b) *n*-hexane agree well with those reported by Ogunronbi et al.[32]

Table A-1. Thermophysical Properties of the Materials.

Thermophysical properties of *n*-pentane   ref

μ (g mol^{-1})	72.15	71
T_c (K)	469.7	71
$T_{\text{triple point}}$ (K)	143.48	72
ρ_l (g cm^{-3})	$0.232\{1 + 1.177555\left(1 - \dfrac{T}{T_c}\right)^{1/3} + 3.891572\left(1 - \dfrac{T}{T_c}\right)^{2/3} - 5.508958\left(1 - \dfrac{T}{T_c}\right) +$	72
p_e (kPa)	$101.325 \cdot \exp\left(\left(1 - \dfrac{309.209}{T}\right) \cdot \exp\left(2.73425 - 1.966544 \times 10^{-3}T + 2.408406\right.\right.$	73
$c_p(T)$ (J mol^{-1} K^{-1})	$86.389058 + 163.62772 \dfrac{\left(\dfrac{1404.5312}{T}\right)^2 \cdot \exp\left(-\dfrac{1404.5312}{T}\right)}{\left(1 - \exp\left(-\dfrac{1404.5312}{T}\right)\right)^2} + 125.55904$ $\dfrac{(\dfrac{3247.1465}{T})^2 \cdot \exp\left(-\dfrac{3247.1465}{T}\right)}{(1 - \exp\left(-\dfrac{3247.1465}{T}\right))^2}$	73
ΔH_{vap} (J mol^{-1})	$R \cdot \exp\left(2.73425 - 1.966544 \times 10^{-3}T + 2.408406 \times 10^{-6}T^2\right) \cdot [309.209 + T($ $\left. -1.966544 \times 10^{-3} + 2 \times 2.408406 \times 10^{-6}T\right)]$	73

c_{pl} (J g^{-1} K^{-1})	2.32 (at 298.15 K)	71

Thermophysical properties of n-hexane | ref

μ (g mol^{-1})	86.18	71
T_c (K)	507.9	71
$T_{\text{triple point}}$ (K)	177.87	72
ρ_l (g cm^{-3})	$0.234\{1 + 1.597561\left(1 - \dfrac{T}{T_c}\right)^{1/3} + 1.842657\left(1 - \dfrac{T}{T_c}\right)^{2/3} - 1.72631\left(1 - \dfrac{T}{T_c}\right) + ($ $+ 0.6463138(1 - \dfrac{T}{T_c})^{5/3}$	72
ρ_s (g cm^{-3})	0.9	74
p_e (kPa)	$101.325 . \exp\left(\left(1 - \dfrac{341.863}{T}\right) \cdot \exp\left(2.79797 - 2.022083 \times 10^{-3} T + 2.287564\right.\right.$	73
$c_p(T)$ (J mol^{-1} K^{-1})	$101.85997 + 196.40919 \dfrac{\left(\dfrac{1400.5301}{T}\right)^2 \cdot \exp\left(-\dfrac{1404.5301}{T}\right)}{\left(1 - \exp\left(-\dfrac{1404.5301}{T}\right)\right)^2} + 137.69426$ $\dfrac{\left(\dfrac{3214.2702}{T}\right)^2 \cdot \exp\left(-\dfrac{3214.2702}{T}\right)}{\left(1 - \exp\left(-\dfrac{3214.2702}{T}\right)\right)^2}$	73

ΔH_{vap} (J mol⁻¹)	$R \cdot \exp\left(2.79797 - 2.022083 \times 10^{-3}T + 2.287564 \times 10^{-6}T^2\right) \cdot [341.863 + T($ $-2.022083 \times 10^{-3} + 2 \times 2.287564 \times 10^{-6}T)]$	73
c_{pl} (J g⁻¹ K⁻¹)	2.27 (at 298.15 K)	71
ΔH_{sub} (J g⁻¹)	151.75 (at 177.84 K)	75
ΔH_{sub} (J mol⁻¹)	50800 (at 178 K)	42

Thermophysical properties of CO_2 ref

μ (g mol⁻¹)	40.01	71
ρ_s (g cm⁻³)	1.6	76
$p_{e(s)}$ (kPa)	$100 \times 10^{\wedge}(6.81228 - 1301.779/(T - 3.494))$	77
$p_{e(l)}$ (kPa)	$101.325 \times 10^{\wedge}(-1353.202/T - 8.142537\log T + 6.259156 \times 10^{-3}T + 24.61$	78
$c_p(T)$ (J mol⁻¹ K⁻¹)	$25.92 + 2.930 \times 10^{-2}T + 2.38 \times 10^{-5}T^2$	23
ΔH_{sub} (J mol⁻¹)	$2.303R \times 1301.679T^2/(T - 3.494)^2$	23

Thermophysical properties of Argon   ref

μ (g mol^{-1})	39.948	71
c_p (J mol^{-1} K^{-1})	0.5203 (298.15 K)	71

References

1. C. T. R. Wilson, *Phil. Trans. Roy. Soc. (London)*, 1897, **189**, 265-307.
2. H. R. Pruppacher and J. D. Klett, *Microphysics of Clouds and Precipitation*, D. Reidel, Dordretch, 1978.
3. C. Hoose and O. Moehler, *Atmospheric Chemistry and Physics*, 2012, **12**, 9817-9854.
4. B. J. Murray, T. W. Wilson, S. Dobbie, Z. Cui, S. M. R. K. Al-Jumur, O. Moehler, M. Schnaiter, R. Wagner, S. Benz, M. Niemand, H. Saathoff, V. Ebert, S. Wagner and B. Kaercher, *Nature Geoscience*, 2010, **3**, 233-237.
5. P. E. Wagner, D. Kaller, A. Vrtala, A. Lauri, M. Kulmala and A. Laaksonen, *Physical Review E*, 2003, **67**.
6. A. Kupc, P. M. Winkler, A. Vrtala and P. Wagner, *Aerosol Science and Technology*, 2013, **47**, I-IV.
7. P. M. Winkler, G. Steiner, A. Vrtala, G. P. Reischl, M. Kulmala and P. E. Wagner, *Aerosol Science and Technology*, 2011, **45**, 493-498.
8. S. Schobesberger, P. M. Winkler, T. Pinterich, A. Vrtala, M. Kulmala and P. E. Wagner, *Chemphyschem*, 2010, **11**, 3874-3882.
9. P. M. Winkler, A. Hienola, G. Steiner, G. Hill, A. Vrtala, G. P. Reischl, M. Kulmala and P. E. Wagner, *Atmospheric Research*, 2008, **90**, 187-194.
10. P. M. Winkler, G. Steiner, A. Vrtala, H. Vehkamaki, M. Noppel, K. E. J. Lehtinen, G. P. Reischl, P. E. Wagner and M. Kulmala, *Science*, 2008, **319**, 1374-1377.
11. P. M. Winkler, A. Vrtala and P. E. Wagner, *Atmospheric Research*, 2008, **90**, 125-131.
12. V. Abdelsayed and M. S. El-Shall, *Journal of Chemical Physics*, 2014, **141**.
13. E. R. Buckle and A. A. Pouring, *Nature*, 1965, **208**, 367-&.
14. A. A. Pouring, *Mechanical Engineering*, 1970, **92**, 70-&.
15. M. Heiler, Üniversität Karlsruhe, 1999.
16. H. L. Jaeger, E. J. Willson, P. G. Hill and K. C. Russell, *Journal of Chemical Physics*, 1969, **51**, 5380-+.
17. P. M. Sforza, A. Castrogiovanni and R. Voland, *Applied Thermal Engineering*, 2012, **49**, 154-160.
18. A. Karimi and M. A. Abdi, *Chemical Engineering and Processing*, 2009, **48**, 560-568.
19. V. Alfyorov, L. Bagirov, L. Dmitriev, V. Feygin, S. Imayev and J. R. Lacey, *Oil & Gas Journal*, 2005, **103**, 53-58.
20. N. Sipocz, A. Hernandez-Nogales, M. A. Gonzalez-Salazar, R. Shisler and V. Lissianski, *Energy Procedia*, 2013, **37**, 1228-1238.
21. V. Balepin, *Supersonic Post-combustion Inertial CO2 Extraction System, Final Report, DOE-OA-13122*, Alliant Techsystems Operations LLC, 2017.
22. M. Betting and H. Epsom, *World oil*, 2007, **228**, 197-200.
23. S. Tanimura, Y. Park, A. Amaya, V. Modak and B. E. Wyslouzil, *Rsc Advances*, 2015, **5**, 105537-105550.
24. N. H. Fletcher, *Journal of Chemical Physics*, 1958, **29**, 572-576.

25.   M. A. Beno, G. Jennings, M. Engbretson, G. S. Knapp, C. Kurtz, B. Zabransky, J. Linton, S. Seifert, C. Wiley and P. A. Montano, *Nuclear Instruments & Methods in Physics Research Section a-Accelerators Spectrometers Detectors and Associated Equipment*, 2001, **467**, 690-693.

26.   G. V. Schulz, *Zeitschrift Fur Physikalische Chemie-Abteilung B-Chemie Der Elementarprozesse Aufbau Der Materie*, 1939, **43**, 25-46.

27.   M. Kotlarchyk and S. H. Chen, *Journal of Chemical Physics*, 1983, **79**, 2461-2469.

28.   V. P. Modak, H. Pathak, M. Thayer, S. J. Singer and B. E. Wyslouzil, *Physical Chemistry Chemical Physics*, 2013, **15**, 6783-6795.

29.   V. P. Modak, A. J. Amaya and B. E. Wyslouzil, *Physical Chemistry Chemical Physics*, 2017, **19**, 30181-30194.

30.   S. Tanimura, Y. Zvinevich and B. Wyslouzil, E, *Journal of Chemical Physics*, 2005, **122**, 194304.

31.   H. Pathak, J. Wolk, R. Strey and B. E. Wyslouzil, *Journal of Chemical Physics*, 2014, **140**.

32.   K. E. Ogunronbi, A. Sepehri, B. Chen and B. E. Wyslouzil, *Journal of Chemical Physics*, 2018, **148**.

33.   K. Duff, Sc.D., Massachusetts Institute of Technology, 1966.

34.   D. Ghosh, D. Bergmann, R. Schwering, J. Woelk, R. Strey, S. Tanimura and B. Wyslouzil, E, *Journal of Chemical Physics*, 2010, **132**, 024307.

35.   E. K. Lang, K. J. Knox, C. C. Wang and R. Signorell, *Planetary and Space Science*, 2011, **59**, 722-732.

36.   E. K. Lang, K. J. Knox, T. Momose and R. Signorell, *Journal of Physical Chemistry A*, 2013, **117**, 11745-11759.

37.   E. K. Lang, K. J. Knox and R. Signorell, *Planetary and Space Science*, 2013, **75**, 56-68.

38.   M. T. Ho, G. W. Allinson and D. E. Wiley, *International Journal of Greenhouse Gas Control*, 2011, **5**, 49-60.

39.   G. Kroner, H. Fuchs, R. Tatschl and O. Glatter, *Particle & Particle Systems Characterization*, 2003, **20**, 111-123.

40.   Y. L. Lin, R. D. Farley and H. D. Orville, *Journal of Climate and Applied Meteorology*, 1983, **22**, 1065-1092.

41.   A. Korolev, *Journal of the Atmospheric Sciences*, 2007, **64**, 3372-3375.

42.   A. Bondi, *Journal of Chemical & Engineering Data*, 1963, **8**, 371-381.

43.   H. Pathak, K. Mullick, S. Tanimura and B. E. Wyslouzil, *Aerosol Science and Technology*, 2013, **47**, 1310-1324.

44.   S. Wildeman, S. Sterl, C. Sun and D. Lohse, *Physical Review Letters*, 2017, **118**.

45.   P. R. Field, R. P. Lawson, P. R. A. Brown, G. Lloyd, C. Westbrook, D. Moisseev, A. Miltenberger, A. Nenes, A. Blyth, T. Choularton, P. Connolly, J. Buehl, J. Crosier, Z. Cui, C. Dearden, P. DeMott, A. Flossmann, A. Heymsfield, Y. Huang, H. Kalesse, Z. A. Kanji, A. Korolev, A. Kirchgaessner, S. Lasher-Trapp, T. Leisner, G. McFarquhar, V. Phillips, J. Stith and S. Sullivan, *Ice Formation and Evolution in Clouds and Precipitation: Measurement and Modeling Challenges*, 2017, **58**.

46.   A. Lauber, A. Kiselev, T. Pander, P. Handmann and T. Leisner, *Journal of the Atmospheric Sciences*, 2018, **75**, 2815-2826.

47. J. C. Earnshaw and C. J. Hughes, *Physical Review A*, 1992, **46**, R4494-R4496.

48. B. M. Ocko, X. Z. Wu, E. B. Sirota, S. K. Sinha, O. Gang and M. Deutsch, *Physical Review E*, 1997, **55**, 3164-3182.

49. R. F. Holland and J. R. Nielsen, *Journal of Molecular Spectroscopy*, 1962, **8**, 383-&.

50. Y. Q. Qiu and V. Molinero, *Crystals*, 2017, **7**.

51. G. Cardini, V. Schettino and M. L. Klein, *Journal of Chemical Physics*, 1989, **90**, 4441-4449.

52. R. Disselkamp and G. E. Ewing, *Journal of Chemical Physics*, 1993, **99**, 2439-2448.

53. R. Signorell, *Molecular Physics*, 2003, **101**, 3385-3399.

54. R. Signorell and M. K. Kunzmann, *Chemical Physics Letters*, 2003, **371**, 260-266.

55. R. Signorell, *Journal of Chemical Physics*, 2003, **118**, 2707-2715.

56. A. Bonnamy, M. Jetzki and R. Signorell, *Chemical Physics Letters*, 2003, **382**, 547-552.

57. A. Bonnamy, R. Georges, E. Hugo and R. Signorell, *Physical Chemistry Chemical Physics*, 2005, **7**, 963-969.

58. R. Signorell, M. Jetzki, M. Kunzmann and R. Ueberschaer, *Journal of Physical Chemistry A*, 2006, **110**, 2890-2897.

59. G. Firanescu, D. Luckhaus and R. Signorell, *Journal of Chemical Physics*, 2008, **128**.

60. O. F. Sigurbjornsson, G. Firanescu and R. Signorell, *Annual Review of Physical Chemistry*, 2009, **60**, 127-146.

61. O. F. Sigurbjornsson, G. Firanescu and R. Signorell, *Physical Chemistry Chemical Physics*, 2009, **11**, 187-194.

62. C. C. Wang, P. Zielke, O. F. Sigurbjornsson, C. R. Viteri and R. Signorell, *Journal of Physical Chemistry A*, 2009, **113**, 11129-11137.

63. M. Nachbar, D. Duft, T. P. Mangan, J. C. G. Martin, J. M. C. Plane and T. Leisner, *Journal of Geophysical Research-Planets*, 2016, **121**, 753-769.

64. K. Dingilian, personal communication.

65. P. C. Mahata and D. J. Alofs, *Journal of the Atmospheric Sciences*, 1975, **32**, 116-122.

66. T. W. Wilson, B. J. Murray, R. Wagner, O. Mohler, H. Saathoff, M. Schnaiter, J. Skrotzki, H. C. Price, T. L. Malkin, S. Dobbie and S. Al-Jumur, *Atmospheric Chemistry and Physics*, 2012, **12**, 8611-8632.

67. D. A. Knopf, P. A. Alpert and B. B. Wang, *Acs Earth and Space Chemistry*, 2018, **2**, 168-202.

68. M. Sokuler, G. K. Auernhammer, M. Roth, C. J. Liu, E. Bonaccurso and H. J. Butt, *Langmuir*, 2010, **26**, 1544-1547.

69. F. Eslami and J. A. W. Elliott, *Journal of Physical Chemistry B*, 2011, **115**, 10646-10653.

70. L. H. Yang, X. J. Quan, P. Cheng and Z. M. Cheng, *International Journal of Heat and Mass Transfer*, 2014, **78**, 460-467.

71. D. Lide, *CRC Handbook of Chemistry and Physics*, CRC Press LLC, Boca Raton, FL, 84th Edition edn., 2003.

72. I. Cibulka, *Fluid Phase Equilibria*, 1993, **89**, 1-18.

73. K. Ruzicka and V. Majer, *Journal of Physical and Chemical Reference Data*, 1994, **23**, 1-39.

74. R. Boese, H. C. Weiss and D. Blaser, *Angewandte Chemie-International Edition*, 1999, **38**, 988-992.

75. D. R. Douslin and H. M. Huffman, *Journal of the American Chemical Society*, 1946, **68**, 1704-1708.

76. D. Newitt, M. Pai, N. Kuloor and J. Huggill, in *Thermodynamic functions of gases*, ed. F. Din, Butterworths Scientific Publications   London, 1956, vol. 1.

77. National Institute of Standards and Technology, http://webbook.nist.gov/chemistry.

78. A. Michels, T. Wassenaar, T. Zwietering and P. Smits, *Physica*, 1950, **16**, 501-504.

Table of contents graphic
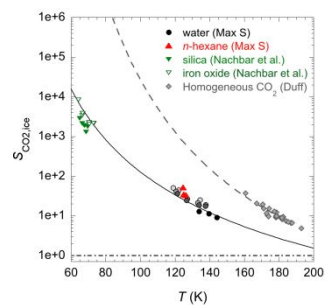
CO$_2$ heterogeneous nucleation starts close to the extrapolated vapor–liquid line for all solid nanoparticles examined to date.